Manganese Mobility in Gale Crater, Mars: Leached Bedrock and Localized Enrichments

J. A. Berger[1*], P. L. King[2], R. Gellert[3], B. C. Clark[4], V. A. Flood[5], M. A. McCraig[3], D. W. Ming[1], C. D. O'Connell-Cooper[6], M. E. Schmidt[7], L. M. Thompson[6], S. J. V. VanBommel[8], B. Wilhelm[3], A. S. Yen[9].

[1]NASA Johnson Space Center
[2]Research School of Earth Sciences, The Australian National University, Canberra, AUS
[3]University of Guelph, Guelph, CAN
[4]Space Science Institute, Boulder, CO, USA
[5]University of Toronto, Toronto, CAN
[6]University of New Brunswick, Fredericton, CAN
[7]Brock University, St. Catharines, CAN
[8]Washington University, St. Louis, USA
[9]JPL-Caltech, Pasadena, USA
[*]Corresponding author jeffrey.a.berger@nasa.gov

Key Points

- In Gale crater on Mars, manganese is depleted in bedrock and enriched in nodules, veins, and coatings
- Manganese was likely leached by aqueous chemical alteration and concentrated via evaporative brine evolution and diagenesis
- Manganese and iron fractionation in mudstone counter-indicates highly alkaline, reducing, and/or oxidizing fluid conditions

Plain language summary

In Gale crater on Mars, the rover *Curiosity* has discovered evidence of the mobility of the redox-sensitive element manganese. We present results for manganese analyses from *Curiosity*'s Alpha Particle X-ray Spectrometer (APXS), an instrument that measures the elemental compositions of martian materials. In most of the layered sedimentary bedrock, manganese concentrations are about one-half of the average Mars crustal composition (approximated as basaltic soil). Our interpretation of the manganese-depleted bedrock is that the element was leached by chemical processes involving water. In most of the bedrock, manganese was likely removed in fluids, whereas iron was not, indicating that this occurred under relatively moderate aqueous conditions. The rover has also discovered manganese-rich veins, nodules, and dark coatings on rock surfaces. These manganese-rich features are associated with enrichments in iron, phosphorus, chlorine, and/or zinc. We provide a thermochemical model to support the hypothesis that the reduced form of manganese (Mn^{2+}) could have been dissolved in water and concentrated as the water evaporated. Manganese was then deposited in localized features when > 99.99% of the Mn^{2+}-bearing water was removed by evaporation. These findings indicate that manganese was dissolved in Gale crater water and was accessible as a potential chemical energy source for life.

Abstract

In Gale crater on Mars, the rover *Curiosity* has discovered evidence of fluid mobilization of the redox-sensitive element manganese. We present results for Mn from *Curiosity*'s Alpha Particle X-ray Spectrometer (APXS), which show that the average MnO concentration in mudstone-dominated sedimentary units (0.22 wt%) is about one-half of the concentration in the average Mars crust (0.44 wt%). Geochemical trends indicate that Mn in the sedimentary bedrock, most of which has a basaltic provenance, was leached by chemical alteration and dissolution. In >350 vertical meters of mudstone-dominated strata, the apparent leaching of Mn and retention of Fe in Fe-O-H phase(s) resulted in the fractionation of Fe and Mn, indicating relatively moderate Eh-pH fluid conditions that were not highly alkaline, reducing, or oxidizing. Exceptions are fracture-associated, silica-rich haloes where both Mn and Fe were leached by low pH fluids. The rover also discovered Mn-rich veins, nodules, and patchy, dark coatings on rock surfaces, which are variably associated with enrichments in Fe, P, Cl, and/or Zn. These Mn-rich features represent ~1% of the 1,029 APXS measurements acquired over ~25 km of rover traverse. A thermochemical model shows that

dissolved Mn^{2+} could have been concentrated via evaporation, sublimation, and/or freezing. Manganese was then likely precipitated in localized features when > 99.99% of the Mn^{2+}-bearing water was removed from the system. These findings indicate that Mn was mobile in Gale crater and therefore bioavailable as a potential energy source for life.

1. Introduction

The Mars Science Laboratory (MSL) rover, *Curiosity*, has discovered localized manganese enrichments in the sedimentary rocks of Gale crater with the Alpha Particle X-ray Spectrometer (APXS) and ChemCam geochemical instruments (Berger et al., 2020; Lanza et al., 2014, 2016; Thompson et al., 2016, 2020). APXS measurements show that most of the bedrock, however, is lower in Mn by roughly a factor of two compared to the average martian crust (Taylor & McLennan, 2010). Sedimentological, geochemical, and mineralogical evidence in Gale crater indicates that the sediments were deposited in a fluvio-lacustrine system (e.g., Grotzinger et al., 2015; Rampe et al., 2017) where redox reactions may have influenced water chemistry (Hurowitz et al., 2017). Manganese is a redox-sensitive element, and the pathway(s) by which it was mobilized are likely recorded in the sedimentary rocks of Gale crater such that the geochemical conditions in the crater can be constrained. Here, we present APXS results for the occurrence of Mn in Gale crater and propose a pathway for Mn depletion in the bedrock and subsequent enrichment via chemical alteration, concentration in fluids, and precipitation in localized features.

Curiosity's >3100 martian solar day (sol; 24.7 h) traverse in Gale crater has been effectively a transect of ~500 m of flat to gently dipping, bedded sedimentary strata (e.g., Edgar et al., 2020; Grotzinger et al., 2015; Stein et al., 2020). Based primarily on sedimentological and orbital observations, a composite stratigraphic column delineates three different sedimentary groups wherein APXS measurements were acquired: Mount Sharp, Bradbury, and Siccar Point (Figure 1) (e.g., Edgar et al., 2020; Grotzinger et al., 2014, 2015). A simplified version of that stratigraphic column is also apparent in plots of sol versus elemental concentrations from the APXS (Figure 2). The lowermost Bradbury group has a lacustrine mudstone (Sheepbed member) that is overlain by fluvial-alluvial sandstone and conglomerate (Grotzinger et al., 2014; Rice et al., 2017; Williams et al., 2013). The Mount Sharp group contains the Murray and overlying Carolyn Shoemaker formations, which are primarily laminated lacustrine mudstone with minor fluvial-aeolian

sandstone (e.g., Edgar et al., 2020; Grotzinger et al., 2015). The rover's traverse from sol ~2300-3076 was in the informally-named Glen Torridon region, which bridges the Murray and Carolyn Shoemaker formations and is denoted separately herein because Glen Torridon was predicted to be a distinct phyllosilicate-bearing assemblage based on orbital data (Milliken et al., 2010). A capping unit, the Siccar Point group, is primarily a cross-bedded aeolian sandstone that unconformably overlies the Murray formation and Glen Torridon region (S. G. Banham et al., 2018, 2021). The ancient aqueous depositional environments evident in Gale crater are reflected in the compositions of the sedimentary materials because several lines of evidence indicate that elements were mobile in Gale crater fluids (e.g., Berger et al., 2020; Rampe et al., 2017; Thompson et al., 2016, 2020; Yen et al., 2017, 2021). Manganese is among the elements with evidence of mobilization in Gale crater fluids, and this has the potential to constrain ancient geochemical conditions.

2. Methods

The APXS instrument analyzes elemental abundances in geologic samples using a combination of particle-induced X-ray emission spectrometry (PIXE) and X-ray fluorescence (XRF) techniques (Campbell et al., 2012; Gellert et al., 2006, 2009). The arm-mounted instrument is deployed by the rover to within ~2 cm of the target surface. We define "target" as a spot on the surface of a sample that is usually < 4 cm in diameter and is given a name and the coordinates presented in Data Set S1. Radiation emitted from curium-244 radioisotope sources induces characteristic X-rays in the ~2-cm-diameter sampling area, which are counted with a detector and converted into an energy dispersive X-ray spectrum. Major, minor, and selected trace element concentrations for atomic number $Z \geq 11$ are calculated from the relative counts in characteristic X-ray peaks, which correlate to the relative abundance of elements in the specimen (Figure S1). Errors reported here represent uncertainty in precision (2σ) and other instrument effects. Instrument accuracy and typical precision error is shown in Table S1 (Gellert & Clark, 2015). The APXS detection limit for MnO is 500 μg/g (ppm) under typical measurement conditions. Sixteen oxides and elements are reported after assigning oxygen to cations and normalizing to 100 weight percent (wt%). Oxidation state is not measured by the APXS; by convention, sulfur, chlorine, manganese, and iron are reported in weight percent respectively as SO_3, Cl, MnO, and FeO. Considerations such as target

preparation (e.g., brushing, drilling) and measurement conditions (e.g., standoff distance, temperature, duration) are discussed in detail by Berger et al. (2020) and VanBommel et al. (2019).

Of ~1000 total APXS measurements acquired over ~3000 sols (Figure 1; Data Set S1), 200 are omitted from the plots and mean calculations because they are either (1) low quality due to sub-standard statistics or spectral resolution (FWHM Fe K_α >210 eV), (2) have a visible mixture of different materials in the APXS field of view (e.g., Ca-sulfate veins crosscutting silicate bedrock), (3) float (i.e., loose fragments of rock with an indeterminate geologic context having compositions distinct from local bedrock), and/or (4) wind-blown deposits of loose, unconsolidated materials. Of the 1028 APXS measurements, 269 are effectively duplicate measurements of the same target. Multiple measurements of one target are conducted to investigate chemical heterogeneity on the surface (typically over a distance of 1-3 cm) or within fines drilled from depths of up to 5 cm (Berger et al., 2020). APXS rasters are also conducted to deconvolve features that are small with respect to the ~2 cm APXS field of view (VanBommel et al., 2016). The duplicate measurements are included and denoted in Data Set S1 but are not plotted in figures herein because they misrepresent the frequency and distribution of targets; that is, small features such as veins and nodules are often rastered, and the additional measurements do not represent multiple targets with that composition. After the described measurements were omitted, 638 of 1028 are shown in the figures. Mean elemental concentrations in bedrock were calculated with the same omissions, and measurements of diagenetic features (e.g., nodules and veins) were also omitted from mean calculations. All APXS measurements up to sol 3076 are included in Data Set S1.

We consider basaltic soil as an approximation of the average martian crust because analyses from two Viking lander sites and APXS results from four rover sites show that it has a relatively uniform chemical composition (B. C. Clark et al., 1982; Foley et al., 2003; Ming et al., 2008; O'Connell-Cooper et al., 2017; Yen et al., 2005). Herein, we describe elemental concentrations relative to the 12 basaltic soil targets measured in Gale crater (stratigraphic group "soil" in Data Set S1). The soils are distinguished chemically by (1) a molar S/Cl ratio of 3.3 ± 0.2, (2) mean MnO concentration of 0.42 ± 0.04 wt%, and (3) a molar Fe/Mn ratio of 46 ± 2.

3. Results

Curiosity's APXS instrument acquired 1028 measurements of geologic targets along the rover's traverse during sols 0-3076 (Figure 1). The rover's traverse has largely been upsection through a sequence of more or less flat-lying sedimentary strata (e.g., Banham et al., 2018; Edgar et al., 2020; Fedo et al., 2018; Grotzinger et al., 2014, 2015; Stack et al., 2019). Thus, plots of elemental concentrations versus sol provide an approximate chemical profile through the strata of the Bradbury, lower Mt. Sharp (Murray formation and Glen Torridon), and Siccar Point groups (Figure 2). Mean concentrations and ± 2σ are reported for bedrock units and exclude 10 targets with MnO >1 wt%. The APXS results are presented with operating parameters, sample comments, and geologic context in Data Set S1 with an explanation in the supplementary information. In this section, we first discuss the occurrence of Mn in Gale crater using APXS results, and then we discuss the occurrence Cl, P, Zn, and Fe enrichments that are associated with Mn-rich features.

3.1. Manganese occurrence

The three main stratigraphic groups explored by *Curiosity* (Bradbury, Mt. Sharp, and Siccar Point) have distinct ranges in bulk elemental compositions (Berger et al., 2020; Thompson et al., 2016, 2020). The Mn occurrence in the bedrock is also distinct between each sedimentary group, as summarized below and in Figure 2a.

Bradbury Group bedrock: The Bradbury group can be described by three compositional endmembers: basaltic, potassic basalt, and high total alkali (> 5 wt% $Na_2O + K_2O$) (Berger et al., 2020; Thompson et al., 2016; Treiman et al., 2016). The lowermost unit of the Bradbury group, the basaltic Sheepbed mudstone at Yellowknife Bay (McLennan et al., 2013; Vaniman et al., 2014), has lower MnO (0.30 ± 0.08 wt%). In contrast, the overlying basaltic and potassic basalt sandstone and conglomerate contain MnO (0.40 ± 0.30 wt%) at concentrations similar to soil but with larger variability. Fourteen mugearitic clasts, hypothesized to have relatively unaltered igneous compositions, have lower MnO (0.21 ± 0.10 wt%) than the basaltic materials (Schmidt et al., 2014; Thompson et al., 2016).

Mt. Sharp Group bedrock: The Mt. Sharp group includes the Murray and Carolyn Shoemaker formations, and it comprises most of *Curiosity's* traverse from sols 720-3076. The Glen Torridon region (sols 2301-present; Figure 1) contains parts of the Murray and Carolyn Shoemaker

formations, as detailed in Data Set S1. Because preliminary interpretations of Glen Torridon indicate a changing depositional environment possibly related to the overlying sulfate-bearing unit (Milliken et al., 2010), we highlight the Glen Torridon results (sols 2302-3076) separately from the other Mt. Sharp results (sols 720-2301). In the Murray formation and Glen Torridon region, the bulk elemental composition of the bedrock is depleted in Ca and Mg, and enriched in Si, relative to basaltic soil. MnO is consistently depleted (0.22 ± 0.20 wt%) when the Mn-rich nodular, vein, and coating measurements are excluded (MnO > 0.75 wt%). A high-SiO_2 (58-74 wt%) facies typified by the Buckskin target occurs in the Murray formation and has very low MnO (< 0.08 wt%).

Siccar Point Group bedrock: The Stimson formation of the Siccar Point group unconformably overlies the Murray formation (Banham et al., 2018) and has a basaltic, soil-like major element composition (Yen et al., 2017). Similarly, MnO concentrations in the bedrock is soil-like, but with greater variability (0.40 ± 0.21 wt%).

Light-toned alteration haloes (~50 cm wide) are associated with fractures and crosscut the Stimson and Murray formations (Yen et al., 2017) and possibly the Bradbury group (Gabriel et al., 2019). The haloes are depleted in MnO, with concentrations as low as 0.05 wt% (Yen et al., 2017). Haloes are also depleted in Al, Fe, Mg, Zn, Ni, and enriched in Si, Ti, P, and Ca-sulfate (Yen et al., 2017).

Manganese enrichments are limited on *Curiosity*'s traverse and occur in a variety of localized mm-cm scale features that are not a major component of the Gale crater bedrock (Figures 2, 3; Data Set S1; Table S3). Concentrations of MnO are greater than soil (0.42 ± 0.04 wt%) in ~10% of targets, and 12 targets have >1 wt% MnO (Figure S3; Table S3). The Mn-enriched features occur as: (1) veins that crosscut bedrock and are less than 5 cm wide (e.g., Alvord Mountain, Abernethy, Dunbartonshire; Figure 3g, 3h); (2) nodules in bedrock (e.g., Timber Point, Ayton, Groken, Falkirk Wheel; Figure 3i); (3) smooth coatings on rock surfaces (e.g., Stephen, Newport Ledge; Figure 3a, 3b, 3c, 3d); and (4) patchy coatings on rock surfaces (e.g., Jones Marsh; Figure 3e, 3f). All of these features are dark-toned relative to adjacent bedrock, which is particularly apparent after the ChemCam LIBS instrument interacted with the surfaces and removed dust. Examples representative of the different enriched features are presented in Figure 3, and summaries of the measurements with MnO >1 wt% are given in Table S3. Only one nodular Mn-

198 rich target (Groken) was drilled and delivered to CheMin and SAM because the features are
199 typically too small with respect to *Curiosity*'s drill volume and/or could have broken under the
200 force of the drill. Groken results are currently being prepared for publication and preliminary data
201 have been presented (Berger et al., 2021; J. V. Clark et al., 2021; Lanza et al., 2021; Thorpe et al.,
202 2021; Treiman et al., 2021).

203 Because most of the Mn-rich features are small with respect to the APXS ~2 cm field of view,
204 the APXS measurements are typically a mixture of the enriched feature as well as the host bedrock
205 and/or other adjacent phases. For example, the raster of the dark, Mn-, Ca-, and Ge-rich Alvord
206 Mountain vein contains high concentrations of SO_3 (up to 40 wt%) because the vein is a mix of
207 different amounts two phases that both were contained in the APXS field of view: (1) dark Mn-
208 rich material and (2) white Ca-sulfate (Berger et al., 2017; VanBommel et al., 2017). As a result,
209 many of the APXS measurements of Mn-rich features are not exactly representative of the feature
210 alone and are minimum concentrations.

211 The ChemCam instrument, a laser induced breakdown spectrometer (LIBS) on the rover's mast
212 (Wiens et al., 2013), has also detected Mn enrichments (Lanza et al., 2014, 2016; Gasda et al.,
213 2018). In general, the stratigraphic locations where Mn enrichments were found by ChemCam
214 correspond with those found by the APXS (Figure S2) (Lanza et al., 2014, 2016; Gasda et al.,
215 2018). Some of the Mn-rich targets were analyzed by both the APXS and ChemCam instruments
216 (e.g., Stephen, Newport Ledge) (Lanza et al., 2016). A larger number of localized Mn enrichments
217 were found by ChemCam than by the APXS, which is likely due to two considerations. First,
218 ChemCam has probed 3–4 times more unique targets than the APXS, and ChemCam has been
219 used to investigate a larger number of heterogenous features than the APXS (e.g., Nachon et al.,
220 2014, 2017). Second, ChemCam shots are ~350 μm in diameter and progressively ablate material
221 with typically ~30 LIBS shots per spot, whereas the APXS FOV is ~2 cm in diameter and the
222 sampling depth increases with atomic number Z from ~3 μm (Na) to ~90 μm (Fe) (e.g., Schmidt
223 et al., 2018). ChemCam is therefore more likely to detect sub-mm enrichments that may not be
224 readily identifiable in standard analyses of APXS data due to the difference in sampling volume
225 (e.g., L'Haridon et al., 2020). Because the sampling volume of ChemCam and APXS is
226 significantly different, we do not make direct comparisons here. In addition, several elemental
227 correlations we discuss in this work (S, Cl, P, Zn) are not possible to evaluate using ChemCam

data due to significantly higher detection limits and accuracy uncertainty (e.g., Forni et al., 2015; Lasue et al., 2016; Wiens et al., 2013).

3.2. Other elemental characteristics of manganese-rich features

Manganese enrichments are commonly accompanied by high concentrations of Cl, P, Zn and/or Fe, which are elements that were also mobile in Gale crater because high concentrations are often associated with veins, nodules, and coatings interpreted to be diagenetic (e.g., Berger et al., 2017, 2020). There is abundant evidence of S mobility, particularly in the white Ca-sulfate veins that crosscut nearly every unit, but there is no apparent correlation of S with Mn. The lack of correlation between Mn and S is notable because rocks with very high MnO (~3.5 wt%) and SO_3 (~35 wt%) were found by the rover *Opportunity* on the rim of Endeavor crater (Arvidson et al., 2016). Below, we present results for Cl, P, Zn, and Fe, first giving an overview of bedrock concentrations for each element, then summarizing enrichments that occur in Mn-rich features.

3.2.1. Chlorine

In the Gale crater bedrock, in general there is no clear correlation between Mn and Cl. Chlorine varies (1.27 ± 0.94 wt%; Figure 2b), with the lowest concentration found in the Buckskin drill fines (0.28 ± 0.01 wt%). Drilled targets show that the top ~1 mm of the bedrock surface is enriched in Cl: the median Cl concentration in drilled material from a few cm below the surface (0.56 wt%) is about half of the median Cl concentration in unbrushed surfaces (1.23 wt%) and brushed surfaces (1.06 wt%) (Berger et al., 2020). Evolved gas analyses (EGA) of drilled samples in the SAM instrument indicate that a fraction of the Cl in the bedrock is within mixed oxychlorine species (Mg-, Ca-, Na-, and/or K-chlorate or perchlorate) (Sutter et al., 2018). Chlorine-bearing phases were detectable with CheMin XRD only as a minor amount of halite (1 wt%) in one of the Murray formation mudstone samples (Quela) (Achilles et al., 2020). SAM and CheMin analyses cannot account for the total Cl measured by the APXS, and a fraction of Cl likely is in the X-ray amorphous fraction that comprises ~20-50 wt% of all drilled samples (Achilles et al., 2020; Morrison et al., 2018; Sutter et al., 2018).

Notable Cl concentrations occur in some, but not all of the Mn-rich targets. Chlorine concentrations are very enriched in Stephen and Jones Marsh (3.1-3.4 wt%) and elevated in Abernethy and Dunbartonshire (1.8-2.0 wt%; Figure 3; Figure 4a, 4b). Stephen has been

interpreted to be the eroded remnant of a vein next to the potassic basalt sandstone Windjana (Figure 3a, 3b) (Lanza et al., 2016). Jones Marsh is a patchy, ~2-mm-thick coating (or crust) on the surface of Murray formation bedrock (Figure 3e, 3f). Abernethy and Dunbartonshire have similar morphologies consistent with erosion-resistant veins (Figure 3g, 3h). All four of these Mn- and Cl-rich targets also have enrichment in either P, Zn, or Fe as described below.

3.2.2. Phosphorus

In the bedrock, P_2O_5 ranges from 0.48 to 2.5 wt% with a soil-like mean concentration of 0.95 ± 0.58 wt% and there are no clear correlations between Mn and P (Figure 2c; Figure 4c, 4d). Minor amounts of fluorapatite (<4 wt%) were identified by CheMin in eight mudstone and sandstone samples (Achilles et al., 2020; Rampe et al., 2017; Yen et al., 2017). In samples with fluorapatite, not all of the P is accounted for in the crystalline phase and a fraction is thus associated with the X-ray amorphous material, as it is in other drilled samples (Rampe et al., 2020). One exception where Mn and P are negatively correlated is in fracture-associated alteration haloes in the cross-bedded Stimson sandstone (Figure S4). The Si-rich haloes are depleted in MnO by up to 90% and enriched in P_2O_5 by up to 65% relative to the host bedrock. No crystalline P-bearing phases were detected in drilled samples of two haloes by CheMin, thus the P is probably associated with the X-ray amorphous material in the haloes (Yen et al., 2017).

Seven of the 12 targets with enriched Mn (> 1 wt%; Table S3) have P enrichments (Figure 4c). Jones Marsh, which also has high Cl (3.10 ± 0.09 wt%), also has a notable P_2O_5 concentration of 7.56 ± 0.40 wt%. Phosphorus-rich features with elevated Mn that have been discovered by the APXS are limited to two locations on *Curiosity*'s traverse: (1) the vicinity of the Sutton Island/Blunt's Point member contact within a ~500 m segment of the traverse (Cliffside Bridge, Timber Point, Berry Cove, Maple Spring, and Jones Marsh) and (2) the Mary Anning and Groken drill site in the Glen Torridon region (Ayton, Falkirk Wheel, Trow, and Groken). The latter four targets are all dark nodules within a ~1 m^2 area where the nodule-bearing Groken target was drilled.

3.2.3. Zinc

Zinc varies widely in the Gale crater bedrock, but it is consistently enriched over most of the traverse in the Bradbury and Mount Sharp groups (1300 ± 700 ppm) compared to soil (300 ± 50 ppm; Figure 2d, 4e, 4f) (Berger et al., 2017). There are three instances where Mn and Zn correlate:

(1) In the Pahrump Hills member of the Murray formation, Mn and Zn correlate negatively with increasing elevation in the laminated mudstone (sols 750-850) (Rampe et al., 2017). (2) Mn and Zn are depleted in fracture-associated haloes, relative to adjacent less-altered bedrock, in the basaltic sandstone of the Stimson formation (Figure S4). (3) Mn and Zn correlate with elevation over two intervals on the traverse, first increasing and then decreasing (sols 1578-1850 and 2300-2520). Drilled samples analyzed by SAM and CheMin have not revealed any additional information on what phase(s) may contain Zn.

Two Mn-rich targets have high Zn: Stephen (8000 ppm) and Newport Ledge (4000 ppm) (Figure 4e, 4f). The two targets both have dark surfaces but different morphologies (Figure 3b, 3d) and occur within very different local bedrock compositions. Stephen is next to the potassic basalt sandstone at the Windjana drill site (Treiman et al., 2016), and has been interpreted to be the fragment of a vein (Lanza et al., 2016), whereas Newport Ledge appears to be a smooth, thin coating on Murray formation sandstone.

3.2.4. Iron

Iron and manganese are not correlated in the Gale crater sedimentary bedrock (Figure 4g, 5a), with two exceptions described below. The basaltic Stimson formation sandstone has soil-like FeO concentrations (19.18 ± 4.6 wt%) and molar Fe/Mn (49 ± 10) (Yen et al., 2017). The Fe/Mn ratio of the soil and Stimson sandstone is approximately the same as that determined for the average martian crust (Taylor & McLennan, 2010) and bulk SNC martian meteorites (Figure 6). The soil-like Fe/Mn value is not shared by the Sheepbed mudstone, Murray formation, or Glen Torridon region (Figure 2e, 5a, 5b), which have respective mean Fe/Mn values of 70, 100, and 110 primarily due to depletion of Mn relative to Fe. Exceptions where FeO and MnO correlate positively are: (1) the Stimson formation fracture-associated haloes, which have lower FeO and MnO due to the apparent leaching of elements during low pH alteration (Yen et al., 2017), resulting in elevated Fe/Mn (Figure 5) and (2) the high-SiO_2 facies of the Pahrump Hills member of the Murray formation that has low FeO and MnO (Buckskin; Figure 5), possibly due to physical dilution by high-silica volcanic detritus (Morris et al., 2016) and/or in situ leaching by fluids (Yen et al., 2021). As a major element in every APXS analysis in Gale crater, FeO is contained within multiple phases, including olivine, pyroxene, magnetite, hematite, jarosite, akaganeite, and the X-ray amorphous material (e.g., Rampe et al., 2020).

The association of Mn and Fe in Mn-rich features varies. Several targets enriched in MnO also have elevated FeO (Newport Ledge, Abernethy, and Dunbartonshire; Figures 2d, 3d, 3h, 4h). However, ~10 targets with notably enriched FeO (>25 wt%; e.g., Morancy Stream, Paradise Hill) have no corresponding MnO enrichment. Conversely, ~10 targets have enriched MnO (0.5-4.0 wt%) but do not contain elevated FeO concentrations; FeO is roughly the same as the bedrock in low-Fe, Mn-rich targets (e.g., Jones Marsh).

4. Discussion

Three key observations emerge from the results presented above:

(1) Most bedrock APXS targets (80%) have Mn concentrations below the average martian crust (0.42 ± 0.04 wt%), and the median Gale crater bedrock (0.23 wt%) is half that of the basaltic Gale crater soil.

(2) A small fraction of all APXS targets are enriched in Mn: (~10%) have MnO concentrations above the range of soil (0.42 ± 0.04 wt%) and ~1% have MnO concentrations >1 wt%. The highest concentrations of Mn are found in nodules, veins, and coatings.

(3) Manganese-enriched targets have one or more enrichments in Fe, P, Cl, and/or Zn, even though these elements comprise a wide range of geochemical characteristics (e.g., ionic charge, solubility, and mineral affinity). There is compelling evidence that all of these elements were variably mobilized by fluids in Gale crater (e.g., Berger et al., 2020).

Below we propose a model that seeks to tie together these three observations, whereby Mn in the bedrock was depleted by chemical alteration of olivine and pyroxene, concentrated in brines via evaporation, sublimation, and/or freezing, and then ultimately precipitated at high concentrations in veins, nodules, and coatings.

4.1. Mn-depleted bedrock

Our interpretation is that the low MnO in the mudstone-dominated sedimentary units is the result of open-system chemical alteration and leaching of Mn from a basaltic precursor. Our reasoning is based on (1) the deduced provenance and (2) the altered characteristics of the rocks, as discussed below.

4.1.1. Bedrock provenance and primary Mn concentrations

The exact provenance of the sediments in Gale crater is unknown, so the Mn content of the protolith(s) is uncertain. However, APXS results provide evidence of bulk chemical similarities between basaltic soil and the mudstone-dominated units (McLennan et al., 2013; Schmidt et al., 2014; Thompson et al., 2016; Yen et al., 2017; Berger et al., 2020). The link between the Sheepbed member mudstone and a basaltic source is based partly on the preservation of the basaltic bulk chemical composition due to nearly isochemical alteration (McLennan et al., 2013; Vaniman et al., 2014). The provenance of the Murray formation and Glen Torridon is less certain because the bulk chemical composition deviates from the average basaltic martian crust, having ~10% higher SiO_2 (48 ± 10 wt%), ~35% lower MgO (5.6 ± 2.2 wt%), ~40% lower CaO (4.3 ± 2.2 wt%), and almost 4 times higher Zn. Berger et al. (2020) used geochemical models of the fractionation and/or crystal sorting via magmatic evolution of rocks with a basaltic mineral assemblage containing olivine, plagioclase, and clinopyroxene (Stanley & Madeisky, 1996) to reason that the Murray formation bedrock has a soil-like basaltic provenance, and that open-system chemical alteration resulted in the depletion of Mg, Ca, and Mn and the passive enrichment of Si in altered residue. The bulk chemical composition of the Glen Torridon bedrock has the same overall chemical characteristics of the Murray formation (Data Set S1) (O'Connell-Cooper et al., 2021), and we extend that interpretation to include the rocks in the region. The mineral assemblage of plagioclase, pyroxene, and Fe-oxides is present in the drilled sediment samples, which is also consistent with a basaltic protolith and/or altered basaltic material (e.g., Rampe et al., 2020). Therefore, the provenance of most of the mudstone-dominated sedimentary units in Gale crater is likely basaltic, having a soil-like composition and primary MnO concentration of 0.42 ± 0.04 wt%.

The basaltic provenance is key for tracing the fate of Mn in the Gale crater sediment because the element occurs as Mn^{2+} via substitution with Fe^{2+} in primary olivine and pyroxene in terrestrial basalts and basaltic martian meteorites (Figure 6) (Papike et al., 2009). Indeed, the consistency of the Fe-Mn systematics of pyroxene and olivine makes Fe/Mn diagnostic of planetary basalts (Papike et al., 2009). In martian meteorites, the mean Fe/Mn of pyroxene and olivine is respectively 33 ± 3 and 50 ± 3 (Figure 6). The mean Fe/Mn of bulk analyses is intermediate: 40 ± 8. The regolith breccia meteorite NWA7034, which has a bulk composition more similar to the APXS analyses on Mars than other meteorites, has a bulk Fe/Mn = of 47 ± 9, and the pyroxenes have the same Fe/Mn as other martian meteorites (Agee et al., 2013). The mean bulk MnO of

basaltic martian meteorites is 0.46 ± 0.07 wt% (Papike et al., 2009), which is effectively the same range of concentrations found in the basaltic soils measured by the Mars Exploration Rover (MER) and MSL APXS instruments (O'Connell-Cooper et al., 2017; Yen et al., 2005).

In summary, the provenance of the mudstone-dominated units is consistent with a basaltic protolith, and the Fe and Mn systematics of martian basalt are well constrained. We therefore conclude that depletions and enrichments in Mn, relative to martian basalt, can be used to trace alteration of the parent materials and mobility of the element in fluids.

4.1.2. Physical sorting during sediment transport?

Because the bedrock units in Gale crater are sedimentary, we ask: can the apparent depletion in Mn be caused during sediment transport by physical *sorting* of basaltic sediment? We can infer the MnO, FeO, and Fe/Mn of the primary Mn-bearing minerals olivine and pyroxene from martian meteorites (Papike et al., 2009) to test this hypothesis. We calculated the likely FeO and Fe/Mn changes caused by physical sorting using the proportions of olivine, pyroxene, and X-ray amorphous material measured in soil by CheMin (Blake et al., 2013), and several hypothetical sorting scenarios are possible (Figure 7). (1) If hydrodynamic sorting caused the removal of the primary Mn-bearing minerals pyroxene and olivine at roughly the same proportions, then the FeO would decrease, and Fe/Mn would increase. (2) If the ratio Px/(Px+Ol) (Px = pyroxene; Ol = olivine) decreased due to olivine accumulation, then FeO and Fe/Mn would increase. (3) If Px/(Px+Ol) increased due to olivine removal, then FeO and Fe/Mn would decrease, reflecting the lower FeO and Fe/Mn of pyroxene. (4) If Px/(Px+Ol) decreased due to pyroxene removal, then FeO and Fe/Mn would increase. These hypothetical sorting trends are not observed in the Gale crater bedrock; Fe/Mn is significantly higher than expected from martian meteorite data and the Fe concentrations are largely within the range of soil (Figure 7). Thus, the depletion of Mn due to the alteration of primary pyroxene and olivine is more plausible than physical sorting as an explanation for low Mn concentrations.

4.1.3. Mn leaching via chemical alteration

Leaching of Mn from bedrock is exemplified by the fracture-associated haloes in Gale crater because the alteration occurred in situ and the bedrock adjacent to the haloes provides an unambiguous parent composition (Yen et al., 2017). Two haloes in the Stimson formation were

403 investigated by drilling four holes: two within ~50-cm-wide light-toned halos around fractures that
404 cross-cut strata (Greenhorn and Lubango), and two in the host bedrock adjacent to the haloes (Big
405 Sky and Okoruso). The haloes are also present in the Murray formation, and one was analyzed by
406 the APXS in a similar fashion by analyzing the light-toned material (Cody) and the adjacent host
407 bedrock (Ferdig). Relative to the host bedrock, the haloes have higher Si, Ti, S, and P and lower
408 Al, Fe, Mn, Mg, Ni, Zn, and Cr (Figures 5 and S4). Aside from the addition of Ca-sulfate (anhydrite
409 and bassanite), all of the crystalline material in the host rock decreases relative to the haloes, and
410 the X-ray amorphous fraction increases ~100-200% (Yen et al., 2017). The likely Mn-bearing
411 mineral pyroxene decreases by ~50-60%; olivine is not present in the parent or the haloes, and if
412 it was present in the parent, it may have been converted to magnetite by oxidative alteration (Yen
413 et al., 2017). The element enrichments and depletions are consistent with alteration by acidic fluids
414 that leached most of the cations, leaving a Si-, Ti-, and P-enriched residue (Yen et al., 2017). The
415 haloes therefore demonstrate that Mn leaching did occur at those locations.

416 The interpreted Mn leaching in the haloes can be extended to the mudstone-dominated
417 sedimentary units. In those units, mobilization and depletion of Mn is also reflected in the passive
418 Si enrichment and depleted Mg and Ca (Berger et al., 2020). Overall, depletion of Mn is most
419 likely tied to the alteration of Mn-bearing olivine and pyroxene. This hypothesis can be tested by
420 examining the relationship between mineralogy and chemistry. Comparing olivine + pyroxene
421 concentrations in the bedrock samples analyzed by CheMin XRD with MnO concentrations
422 (Figure 8a) and Fe/Mn (Figure 8b) shows a plausible correlation between the amount of Mn-
423 bearing crystalline material and elemental Mn concentrations. The haloes, compared to their
424 basaltic parent, are depleted in Mn by ~70% and olivine + pyroxene by ~60%. Assuming the
425 provenance of the lacustrine and fluvio-lacustrine samples is soil-like basaltic material (except for
426 Windjana), depletion in olivine + pyroxene generally correlates with lower Mn. Iron is not depleted
427 in the bedrock samples, thus Fe/Mn increases.

428 Stability models for Mn constrain the Eh and pH conditions under which Mn^{2+} can be soluble
429 in relevant water compositions derived from Snake River Plains Basalt aquifers (Figure 9) (Wood
430 & Low, 1988). Contrasting Fe and Mn stability further constrains likely Eh and pH. Depletion of
431 both Mn and Fe in the haloes indicates that both elements were soluble, which conveniently places
432 limits on the fluid Eh-pH as oxidizing-low pH through reduced, moderate pH values (light blue in
433 Figure 9). Depletion of Mn and retention of Fe in the mudstone suggests an Eh-pH range where

Mn is soluble, but Fe is not (dark blue in Figure 9). That is, upon dissolution of olivine and/or pyroxene, fractionation of Mn and Fe was possible as Mn^{2+} was removed in fluid, whereas Fe remained as a solid oxide/oxyhydroxide/hydroxide/sulfide. This can be compared to results from the Mars *Phoenix* lander's Wet Chemistry Laboratory (WCL) experiment, which determined an Eh of ~300 mV at a pH of 7.7 ± 0.1 for the Rosy Red sample soil solution (Figure 9) (Quinn et al., 2011). Those values place that soil sample in the Eh-pH range where Mn^{2+} is an aqueous phase and Fe^{3+} is within a solid Fe-O-H phase. Given the abundant Fe-oxide minerals detected by CheMin, it is plausible that Mn was mobilized in the Gale crater mudstone, whereas Fe was insoluble, under similar Eh-pH conditions (dark blue in Figure 9).

4.2. Evaporative concentration of Mn

To approximate the fate of Mn in an evaporitic scenario relevant to Gale crater, which is a closed basin (Cabrol et al., 1999), we ran a simple thermochemical evaporation model at 100 kPa and 25 °C utilizing Geochemist's Workbench (GWB) software (Bethke et al., 2020). In a closed basin, dissolved constituents are necessarily deposited as solids when they reach saturation due to water removal by evaporation and/or freezing and sublimation. To simulate the process of brine formation, a dilute starting composition was adapted from analyses of basaltic aquifers in the Snake River Plains Group basalts (SRPB) in Idaho and eastern Oregon, USA (Wood & Low, 1988) (summarized in Tables S4 and S5). The assumptions include (1) charge is balanced by Cl^-, (2) Eh and pH are allowed to change, (3) carbonates do not form until the final step, and (4) the system is closed, except for the removal of pure water as a gas [$H_2O(g)$]. Hematite and the silica polymorphs quartz, cristobalite, and tridymite were suppressed because they are typically inhibited in natural low-temperature systems. Carbonate precipitation was inhibited by decreasing the initial HCO_3^- (~220 mg/L) of the SRPB water to 0.1 mg/L. Carbonate formation (including Ca-, Mg-, Fe-, and Mn-carbonates) was limited in the model because they are not detected >1 wt% in Gale crater rocks and soils measured with CheMin X-ray diffraction (XRD) and SAM EGA (Rampe et al., 2020; Sutter et al., 2018). The resulting HCO_3^-/SO_4^{2-} (~1.5×10^{-3}) is plausible for a S-rich martian system (e.g., Penelope L. King & McLennan, 2010). The model was run in ~62,000 steps to simulate the evaporation of 99.99% of the initial water [reaction: $H_2O(l) \Rightarrow H_2O(g)$], and the minerals precipitated were allowed to react with the evolving solution. Kinetic effects at high ionic strength are not considered in the model. GWB evaporation models that simulated 99.99%

464 evaporation of Mars-relevant solutions have been presented previously (Tosca et al., 2005), and
465 kinetic effects were also assumed to be negligible based on prior work (Harvie et al., 1984). We
466 acknowledge that the modeled pressure and temperature are not appropriate for Mars and that
467 freezing and sublimation also remove pure H_2O; nonetheless, we model evaporation for simplicity
468 and to avoid disequilibrium effects such as brine trapped in ice.

469 The model results for the SRPB fluid are shown in Figure 10, where we present the molality
470 of aqueous Mn species ($\geq 10^{-10}$) and the saturation of Mn-bearing solids. Saturation is represented
471 by Q/K, where Q is the ratio of component activities and K is the ratio of component activities
472 when the fluid is in equilibrium (e.g., Langmuir, 1997). Thus, the solution is saturated with respect
473 to a phase when $Q/K \geq 1$. The evaporation model indicates that the fluid is undersaturated in Mn-
474 bearing solids throughout the 99.99% evaporation, and Mn^{2+} is concentrated in Mn-species in the
475 brine: for example, Mn^{2+}(aq), $MnCl_2$(aq), and $MnCl_3^-$(aq) (Figure 10a). In the simulation, goethite,
476 talc, and hydroxyapatite were supersaturated under all conditions. Amorphous silica is saturated
477 with ~30% of the water remaining, gypsum is saturated with ~3% of the water remaining, and
478 dolomite, halite, and sylvite are saturated in the final step with 0.01% of the water remaining.

479 In summary, this simple evaporation model suggests that it may be possible to concentrate
480 dissolved Mn in a brine within a basaltic aquifer. Manganese remains soluble during evaporation
481 and no Mn minerals are predicted to form after 99.99% evaporation. By testing this simulation, we
482 are not implying that it is a comprehensive model for the processes that concentrated Mn in Gale
483 crater. In particular, it does not account for the substitution of Mn in other minerals common in
484 Gale crater (e.g., magnetite, hematite) (Rampe et al., 2020), nor does it include sorption, which are
485 both processes that could have affected Mn mobility. However, concentration of Mn in brine after
486 dissolution of olivine and/or pyroxene is a plausible process that fits the depleted bedrock and
487 localized enrichments observed by *Curiosity*.

488 **4.3. Precipitation of Mn in localized features**

489 The Mn-bearing phase(s) in the Mn-rich features that *Curiosity* discovered has(have) not been
490 unambiguously identified (cf. Lanza et al., 2016). The occurrence in veins, nodules, and coatings,
491 and co-enrichments in Cl, P, Zn, and Fe (Figure 4) are consistent with concentration and
492 precipitation from fluids. However, the rover's instrumentation is limited and identifying Mn-
493 bearing phases is not straightforward. Nor has it been straightforward to determine if the Mn is

494 adsorbed to surfaces and/or contained within amorphous material, rather than incorporated in
495 crystalline minerals. Most Mn-rich targets have been too small and/or breakable to safely drill and
496 deliver material to CheMin and SAM for XRD and EGA measurements. The exception is the target
497 Groken (sols 2906-2921), which has mm-scale, dark nodules enriched in Mn and P, as determined
498 by a raster of the adjacent nodular target Ayton (Figure 3i, 4c, 4d). The nodule-rich bedrock at the
499 Groken/Ayton site was drilled and analyzed by CheMin and SAM, and preliminary results suggest
500 that the Mn- and P-bearing phase(s) may not be identifiable unambiguously with XRD or EGA,
501 but that EGA indicates Mn may have a 2+ oxidation state (Berger et al., 2021; J. V. Clark et al.,
502 2021; Lanza et al., 2021; Thorpe et al., 2021; Treiman et al., 2021). Despite the ambiguities, we
503 can apply the principle of parsimony to constrain the Mn-rich occurrences, and below we discuss
504 Mn oxidation and possible Mn-bearing phases. We do not consider Mn adsorption to explain the
505 Mn-rich features because that process is unlikely to result in Mn concentrations of more than 1
506 wt% (e.g., Groeningen et al., 2020; Kebabi et al., 2017).

507 Manganese enrichment by oxidation of dissolved Mn^{2+} is remarkable for an aqueous system
508 in Gale crater because, at pH >2 and under Mars's atmosphere, the Mn oxidation reaction to form
509 pyrolusite,

510 $Mn^{2+} + 2H_2O \rightarrow Mn^{IV}O_2 + 4H^+ + 2e^-$ (Eqn. 1)

511 ($E° = -1.23V$),

512 is non-spontaneous and has a negative electrochemical potential (E° at STP). Thus, a strong oxidant
513 is necessary to induce precipitation of Mn as an oxide. Oxychlorine species are strong oxidants
514 and have been identified in Gale crater bedrock (J. V. Clark et al., 2021; Ming et al., 2014; Sutter
515 et al., 2018) and by the Wet Chemistry Laboratory on *Phoenix* (Kounaves et al., 2010, 2014).
516 Specifically, perchlorate ($Cl^{VII}O_4^-$) and chlorate ($Cl^{IV}O_3^{2-}$) were detected by Sutter et al. (2018).

517 In theory, perchlorate oxidizes Mn^{2+} spontaneously:

518 $ClO_4^- + Mn^{II} + 4H^+ + 6e^- \rightarrow Mn^{IV}O_2 + Cl^- + 2H_2O$ (Eqn. 2)

519 ($E° = +0.11V$).

However, perchlorate is kinetically inhibited at low temperatures, and it may be inert as an oxidant, as suggested by experiments with Fe (Mitra & Catalano, 2019). Oxidation by chlorate is favored because the reaction is spontaneous with higher E°:

$$ClO_3^- + Mn^{2+} + 2H^+ + 4e^- \rightarrow Mn^{IV}O_2 + Cl^- + H_2O \quad \text{(Eqn. 3)}$$

(E° = +0.185V).

Chlorate is kinetically reactive at low temperatures; for example, it oxidizes Fe^{2+} in experimental setups at pH 3-7 (Mitra & Catalano, 2019). However, the reaction rate for Eqn. 3 is currently unknown in a natural system.

It is possible that Mn-rich features preserve a primary 2+ oxidation state for Mn in carbonates, chlorides, and/or phosphates. In aqueous systems derived from a basaltic crust and containing HCO_3^- that is buffered to 6.5 < pH < 10.5 by a basaltic mineral assemblage, carbonates reach saturation and can precipitate readily (e.g., King et al., 2004). Evidence of carbonates via C detections (above the atmospheric background) in the Mn-rich features has not been reported (Lanza et al., 2016); however, the detection limit for carbonate may be too high (~20 wt%) to identify carbonates reliably (Anderson et al., 2017). In addition, CheMin has not found carbonates >1 wt% with X-ray diffraction. Mn-chlorides may be possible because two targets are highly enriched in Mn and Cl at a molar ratio (Mn/Cl ~0.62) that is similar to $MnCl_2$ (Mn/Cl = 0.5) (Figure 4a, 4b). Possible phases are anhydrous Mn-chloride ($Mn^{II}Cl_2$) or tetrahydrate Mn chloride ($Mn^{II}Cl_2(H_2O)_4$). Phosphates are another possibility, including Mn-sarcopside ($Mn^{II}_3(PO_4)_2$) or $Mn^{II}HPO_4$. However, the ratio of MnO to P_2O_5 observed in the targets with the highest concentrations of the two oxides does not match the stoichiometry of those Mn-phosphate phases (Figure 4d). A jahnsite-whiteite group mineral has been proposed for the Mn-and P-rich targets, but this interpretation is speculative (Berger et al., 2021; Treiman et al., 2021). Overall, the presence of Fe^{3+} oxides in CheMin samples (Rampe et al., 2020) indicates that late-stage diagenetic fluids in Gale crater were above the hematite-magnetite buffer, and the relevant anionic species do not tend to change appreciably at conditions between hematite-magnetite, unless pH changes. Chlorides and phosphates are possible, but unlikely relative to the solids with other major cations (Fe, Mg, Ca).

We find that there is not one single phase or assemblage of phases that characterizes the Mn enrichments, and that this is consistent with the formation of the features from the evaporation,

sublimation,and/or freezing of a brine with concentrated conservative elements including Mn, Fe, P, Cl, and/or Zn. If a brine or sedimentary system undergoes episodic flooding (water addition) and then re-evaporation even once (let alone tens to millions of times), then more complexity may arise. Indeed, K-Ar dating of jarosite at 2.12 ± 0.36 Ga in a Gale crater mudstone is evidence of post-depositional fluid flow and salt formation as recent as the Amazonian (Martin et al., 2017). The variability of the enrichments over the traverse, even within bedrock having a relatively uniform composition, is also consistent with this interpretation.

5. Conclusions

Our interpretation of the occurrence of Mn in Gale crater, as measured by the APXS, is that Mn was mobile in fluids, as evident in depleted bedrock, depleted alteration haloes, and highly enriched veins, nodules, and coatings. Mn^{2+} was likely released into fluids via alteration of a basaltic precursor, and then subsequently concentrated in brine(s) that resulted from evaporation, sublimation, and/or freezing of Gale crater fluids, such that Mn^{2+} would be enriched when the liquid water was removed. Dissolved Mn species would necessarily precipitate when >99% of the water was removed. This scenario is consistent with the highly localized, Mn-rich veins, nodules, and coatings in Gale crater, which contain widely variable associations of Mn with high concentrations of Fe, Cl, P, and/or Zn. Variability in the Mn-rich features suggests that complex mixtures of phases precipitated from brine(s). It is plausible that the localized enrichments preserve mass balance for Mn in the closed basin of Gale crater because the extensive leaching of Mn from thick sedimentary units may be accounted for in the high-Mn features. Manganese is utilized in reduction-oxidation biochemical reactions as an energy source for life, and thus evidence of Mn mobility in fluids has important implications for habitability in Gale crater.

Acknowledgements

This research was funded by the Canadian Space Agency, NASA-JPL-Caltech, NASA-JSC, USRA NPP, and the Australian Research Council grant DP200100406. The APXS data are archived at the Planetary Data System (MSL APXS RDR dataset: 10.17189/1518757).

Figures

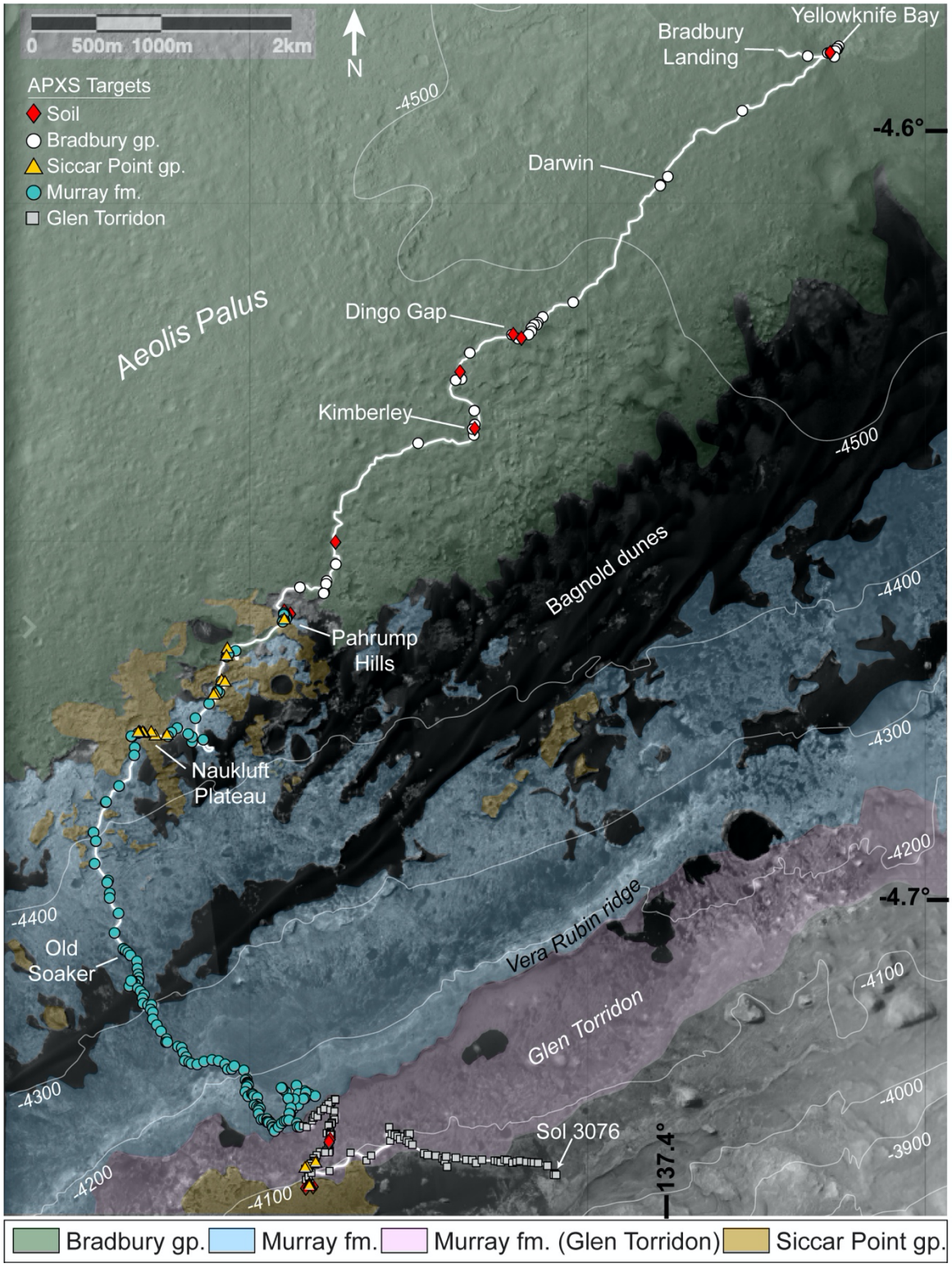

Figure 1: *Curiosity*'s traverse and locations of APXS targets up to sol 3076. The Murray formation and Glen Torridon region make up the Mount Sharp group. The rover's traverse is the white line from Bradbury Landing on sol 0 up to the Nontron drill site on sol 3076 and the APXS symbols correspond with figures in the manuscript. Selected waypoints and outcrop on the traverse are indicated. The geologic units and topographic contour lines are adapted from (Grotzinger et al., 2015).

Figure 2: Plots of (a) Mn, (b) Cl, (c) P_2O_5, (d) Zn, and (e) molar Fe/Mn versus sol (sols 0-3076), covering APXS results over the entire MSL mission from landing up to the Nontron drill site in the Glen Torridon region. Average Gale crater soil ± 2σ is denoted (horizontal brown lines). Selected Mn-rich targets are indicated: Stephen (St), Garden City (GC), Newport Ledge (NL), Timber Point (TPt), Jones Marsh (JM), Abernethy (Ab), Dunbartonshire (D), and Ayton (Ay). See Section 2 for explanation of the data.

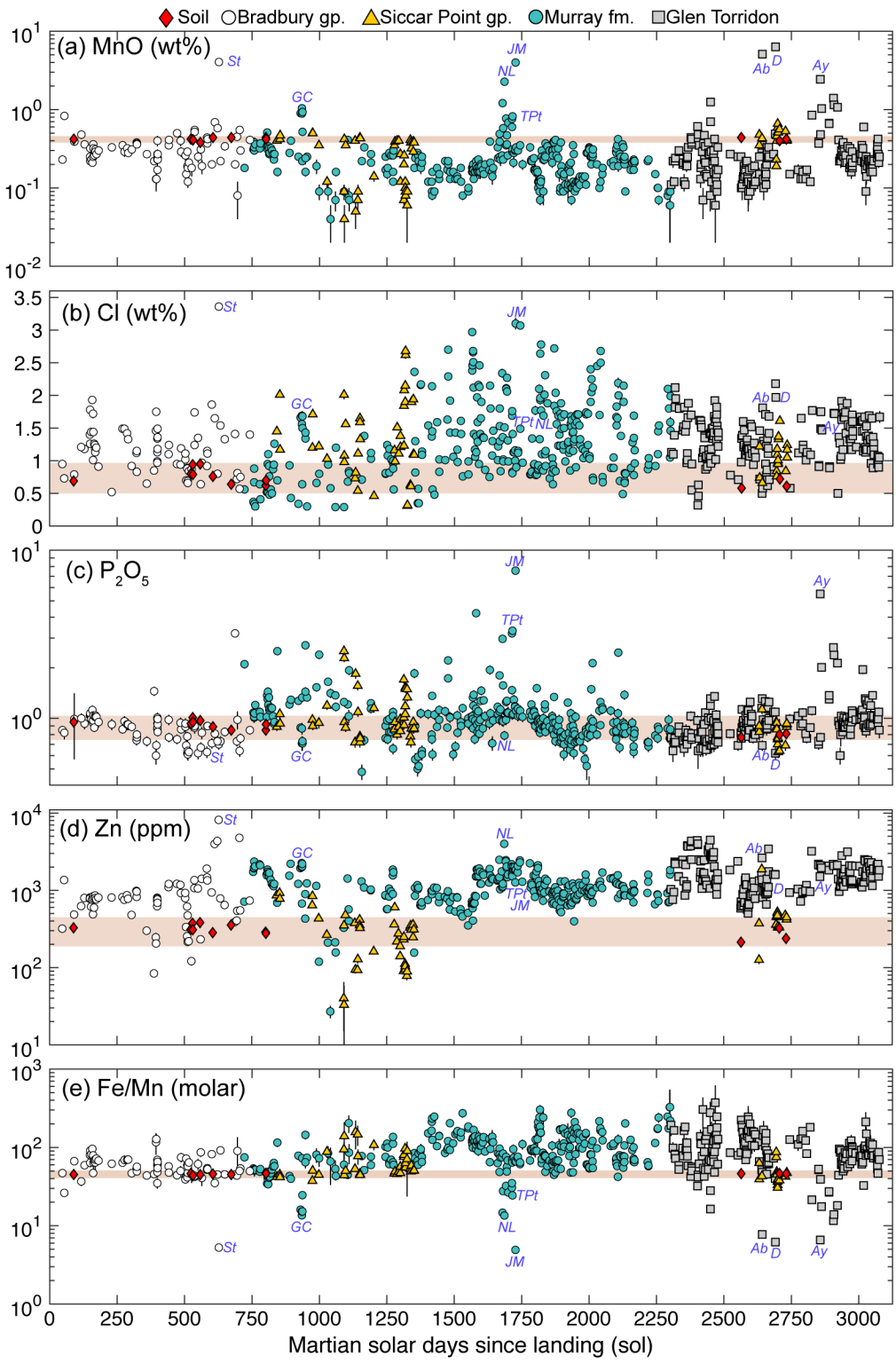

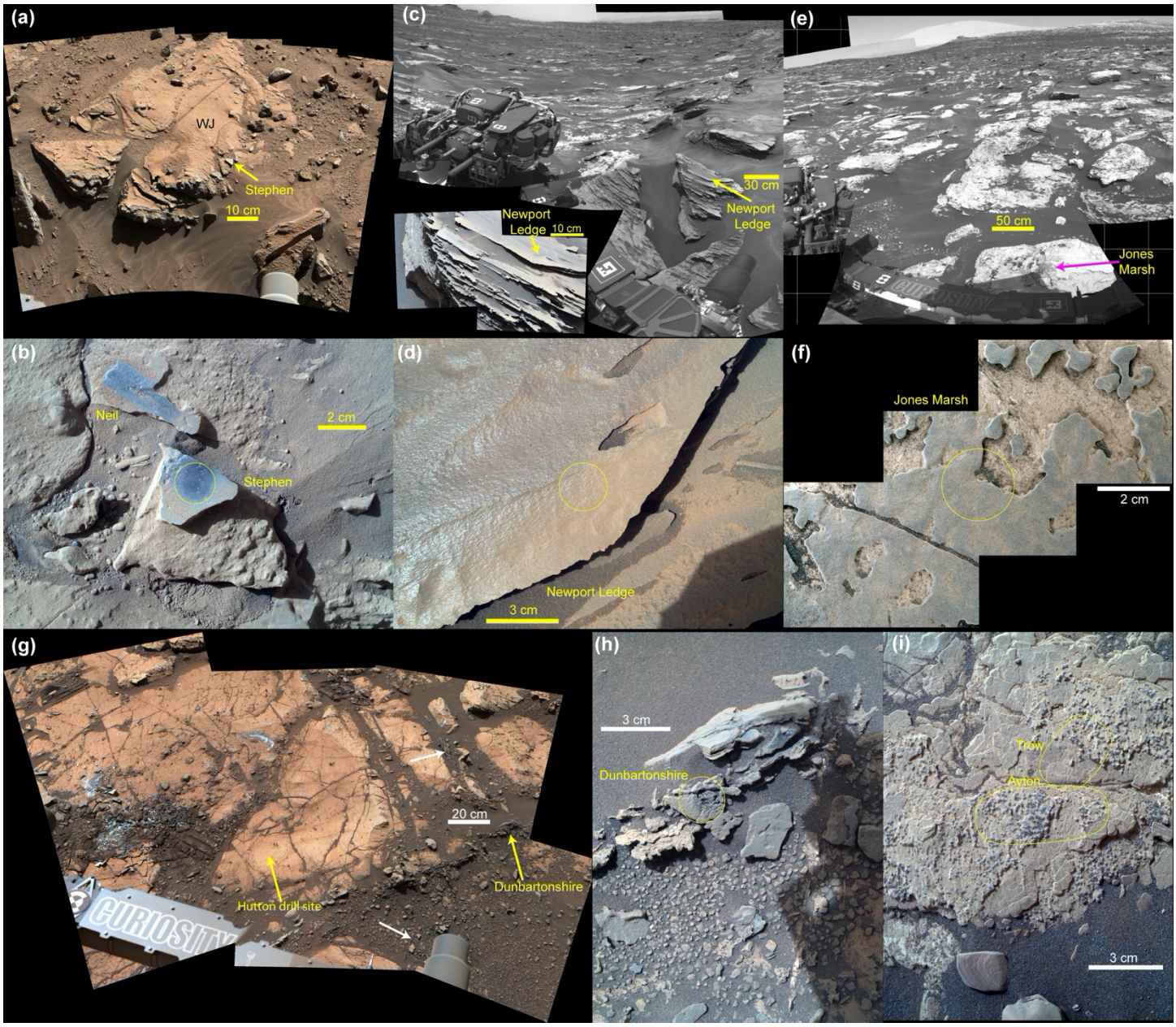

Figure 3: Images of representative Mn-rich targets Stephen, Newport Ledge, Jones Marsh, Dunbartonshire, Ayton, and Trow. Yellow circles in MAHLI images denote the approximate APXS FOV. (a) Mastcam context mosaic of the Windjana drill site (WJ) before drilling, including the Zn-rich target Stephen (MnO = 4.05 ± 0.06 wt%). (b) MAHLI image of Stephen after the dust was removed by ChemCam (the APXS measurement was after dust removal). The adjacent Mn-rich ChemCam target Neil is indicated. The APXS FOV indicates the center of the 5-point APXS raster of the target. (c) Navcam context mosaic of Newport Ledge (MnO = 2.27 ± 0.05 wt%). Mastcam images (inset) show the post-APXS ChemCam analysis of Newport Ledge, which removed dust and exposed the dark surface. (d) MAHLI image of Newport Ledge, which has a relatively continuous coating of dark material. (e) Navcam context mosaic of the P-rich Jones Marsh target (MnO = 3.99 ± 0.09 wt%), a patchy coating of dark material. (f) MAHLI image of Jones Marsh shows the contrast of the patchy dark coating with the lighter-toned bedrock. (g)

642 Mastcam mosaic of the Hutton drill site before drilling, showing Dunbartonshire (MnO = 6.33 ±
643 0.13 wt%) and similar fracture-fill material (white arrows). Dunbartonshire has the highest MnO
644 discovered in Gale crater. (h) MAHLI image of fracture-associated Dunbartonshire. (i) MAHLI
645 image of the Ayton and Trow rasters (MnO up to 2.44 ± 0.05 wt%), which is ~15 cm adjacent to
646 the Groken drill site and is associated with high P_2O_5 (up to 5.49 ± 0.28 wt%). Images details are
647 provided in Table S2.
648

Figure 4: Plots of MnO concentrations versus (a, b) Cl, (c, d) P_2O_5, (e, f) Zn, and (g, h) FeO. The data and notations are the same as described in Figure 2. The left column (a, c, e, g) plots data on a log scale; the right column (b, d, f, h) plots the same data on a linear scale for comparison. Simple addition models for MnO_2, $Mn_3(PO_4)_2$, $MnH(PO_4)$, and $MnCl_2$ are shown as vectors in (a-d). The depletion trends of Mn, Zn, and FeO in the Buckskin-type silica-rich facies and silica-rich fracture haloes is indicated by arrows in (e) and (g). The mugearitic Bradbury group targets have lower MnO and FeO that is attributed to igneous processes, and they are enclosed by a polygon in (g).

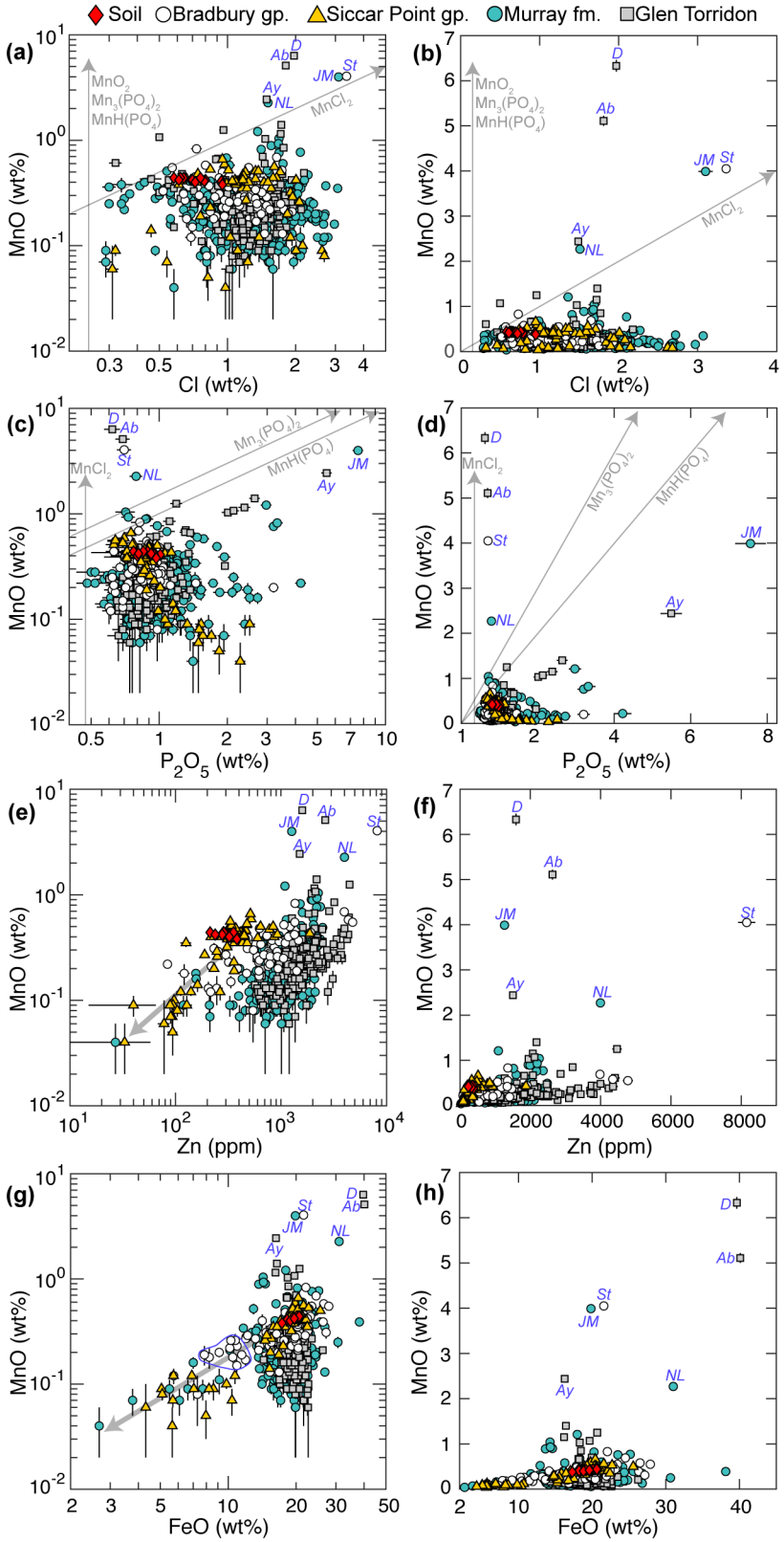

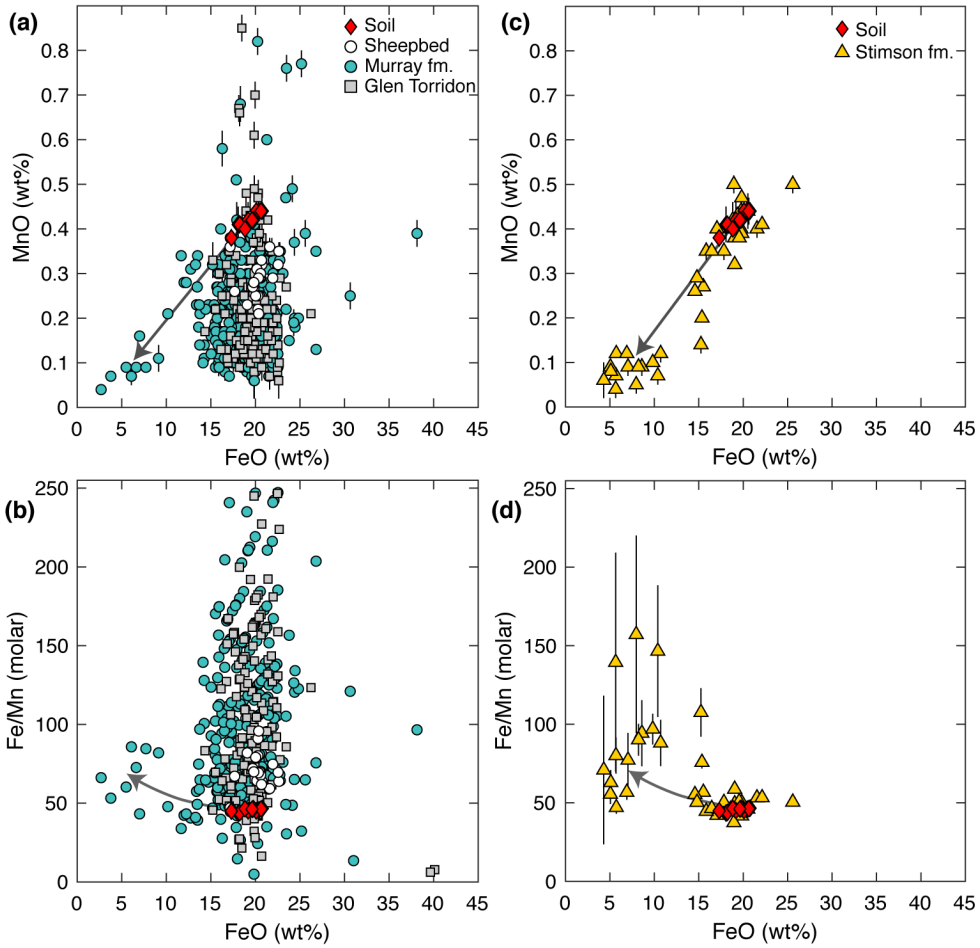

668

669 **Figure 5:** MnO and FeO concentrations in the mudstone-dominated units (a, b) compared to the
670 sandstone of the Stimson formation (c, d). MnO and Fe/Mn versus FeO in (a) and (b) demonstrate
671 that the lesser MnO relative to the basaltic soil does not have a corresponding change in FeO. Two
672 exceptions (arrows) are: (1) the Buckskin high-silica facies, which is a thin (< 5 m thickness) layer
673 in the Pahrump Hills member of the Murray formation and (2) a silica-rich halo (Cody and Ferdig
674 sol 1109). In contrast, MnO depletion in the Stimson formation (c, d) has a corresponding decrease
675 in FeO and a lower magnitude of Fe/Mn increase. The MnO depletion in the Stimson is limited to
676 fracture associated haloes (arrows) (Yen et al., 2017). Error bars are omitted for clarity in (b);
677 typical error for Fe/Mn values above 100 is ~5-10% for overnight integrations and ~15-35% for
678 short integrations and larger standoff measurements. Error for Fe/Mn < 100 is typically smaller
679 than the symbols (3-5%). Ten targets with MnO above 0.9 wt% are not shown in (a) and (b).
680

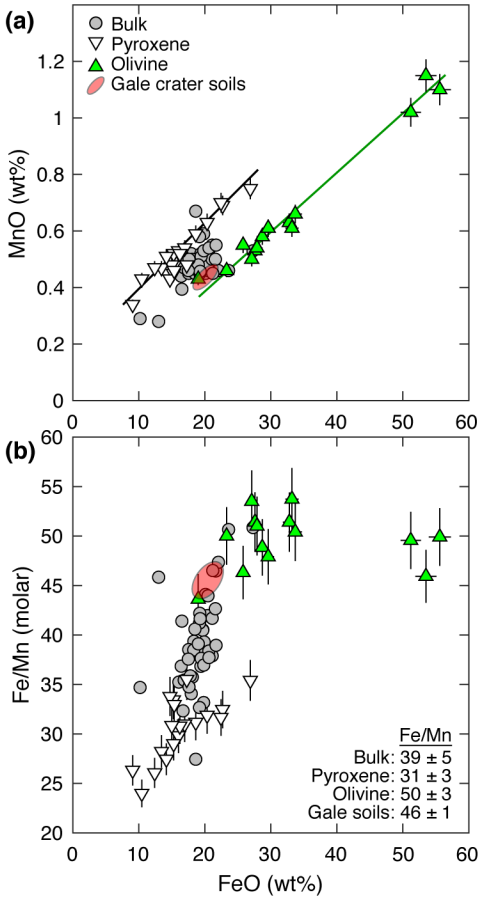

Figure 6: MnO and FeO concentrations in martian meteorites compared to APXS measurements of Gale crater soils on a S- and Cl-free basis. (a) MnO versus FeO and (b) Fe/Mn versus FeO are shown for bulk meteorites and average microprobe analyses of pyroxenes and olivines (Papike et al., 2009). Each pyroxene and olivine point represents ~50 individual analyses of the mineral in one meteorite. The 12 Gale crater soil compositions are enclosed in the red polygon. The Fe/Mn of each group is shown in (b).

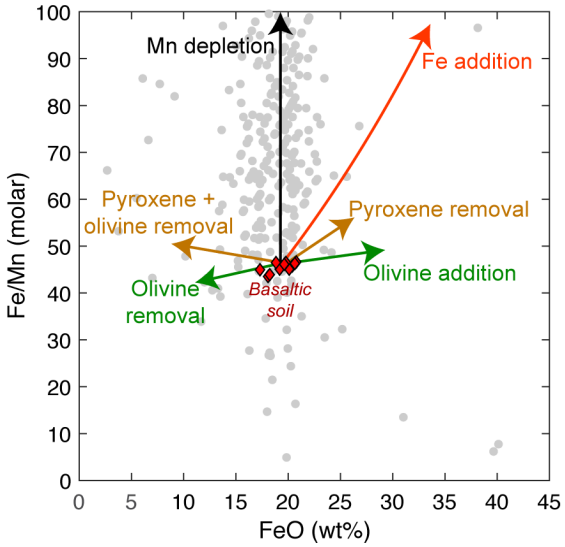

Figure 7: Modeled Fe/Mn and FeO changes under hypothetical conditions that can change Mn concentrations and are relevant to Gale crater. The physical sorting of the principal Mn-bearing phases derived from a soil-like basaltic protolith (pyroxene and olivine) can control changes in FeO content and small changes in Fe/Mn. This would occur if the bulk proportions of the minerals were changed by physical transport processes capable of sorting Mn-bearing phases based on, for example, differences in density or grain size (e.g., Thorpe et al., 2019). Such processes could result in the accumulation (enrichment) or removal (depletion) of Mn-bearing minerals. Addition of Fe as a cement could also result in detectable changes in FeO and Fe/Mn. In contrast, the removal of Mn in solution via olivine and pyroxene dissolution in a system where Fe-oxides are insoluble would result in an increase in Fe/Mn with minimal or zero change in FeO concentrations. We propose that the Mn dissolution model most plausibly fits the observed Fe/Mn and FeO in the mudstone-dominated sedimentary units in Gale crater (Figure 5). Data from Figure 5b are shown for comparison.

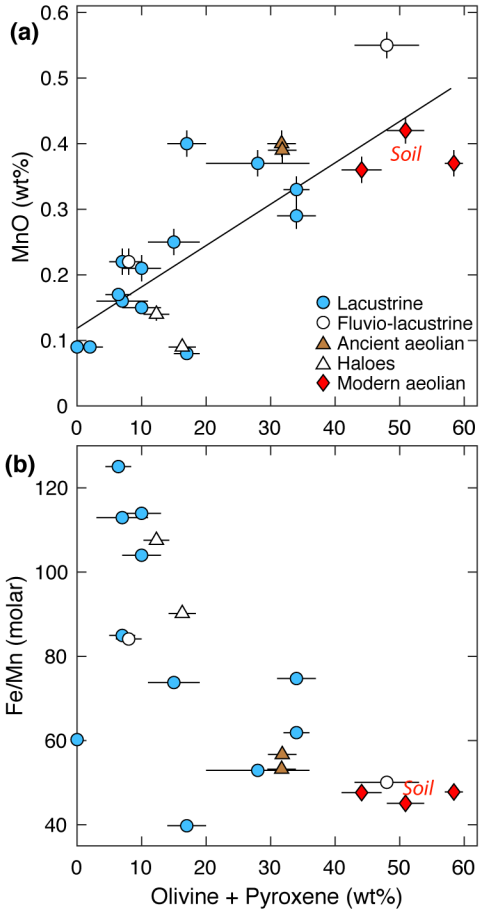

Figure 8: (a) MnO and (b) Fe/Mn versus the sum of olivine and pyroxene in CheMin samples. MnO and the Mn-bearing minerals have a positive linear correlation (R^2 = 0.64). Generally, a decrease in olivine and pyroxene corresponds with an increase in Fe/Mn, but the apparent negative correlation is less certain due to several outliers. The interpreted sedimentary environment of the CheMin samples is denoted (Rampe et al., 2020), and lacustrine samples were in mudstone-dominated units. Mineral abundances are in wt% normalized to 100% without amorphous material. Two samples with high Fe/Mn (~250) are not shown in (b): Marimba and Rock Hall have 2 wt% and 17 wt% olivine + pyroxene, respectively. CheMin data are from (Achilles et al., 2020; Bish et al., 2013; Blake et al., 2013; Rampe et al., 2017; Treiman et al., 2016; Vaniman et al., 2014; Yen et al., 2017).

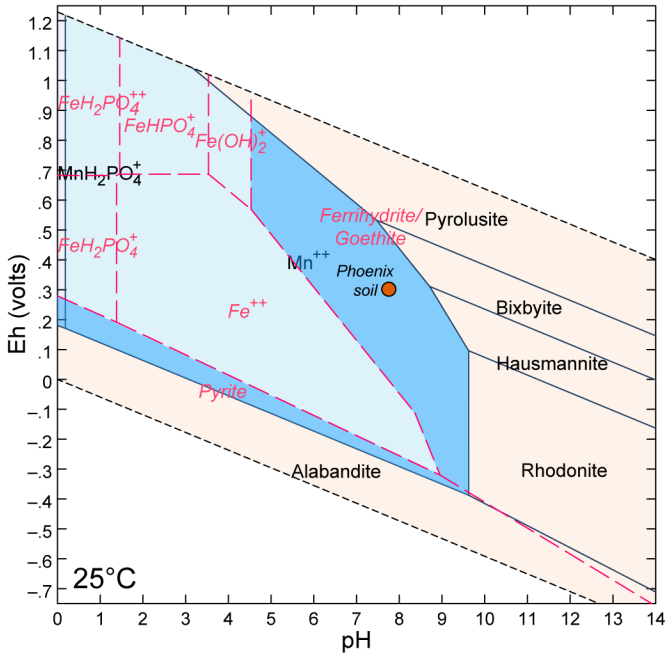

Figure 9: Superimposed Pourbaix diagrams for Mn and Fe with a water composition adapted from analyses of Snake River Plains Basalt aquifers (see Tables S4 and S5 for modeling details). Fields where Mn is stable as solid and aqueous phases are tan and blue, respectively, and the phase is shown in black text. Fe stability fields are denoted by red dashed lines, and Fe phases are shown in red italics. The darker blue field indicates Eh/pH values where Mn is stable as an aqueous phase, whereas Fe is stable as a solid phase; that is, Mn and Fe have the potential to fractionate into respective aqueous and solid phases under these conditions. The Mars Phoenix WCL results for the soil sample Rosy Red is plotted (Eh ~0.3 V; pH ~7.7) (Quinn et al., 2011).

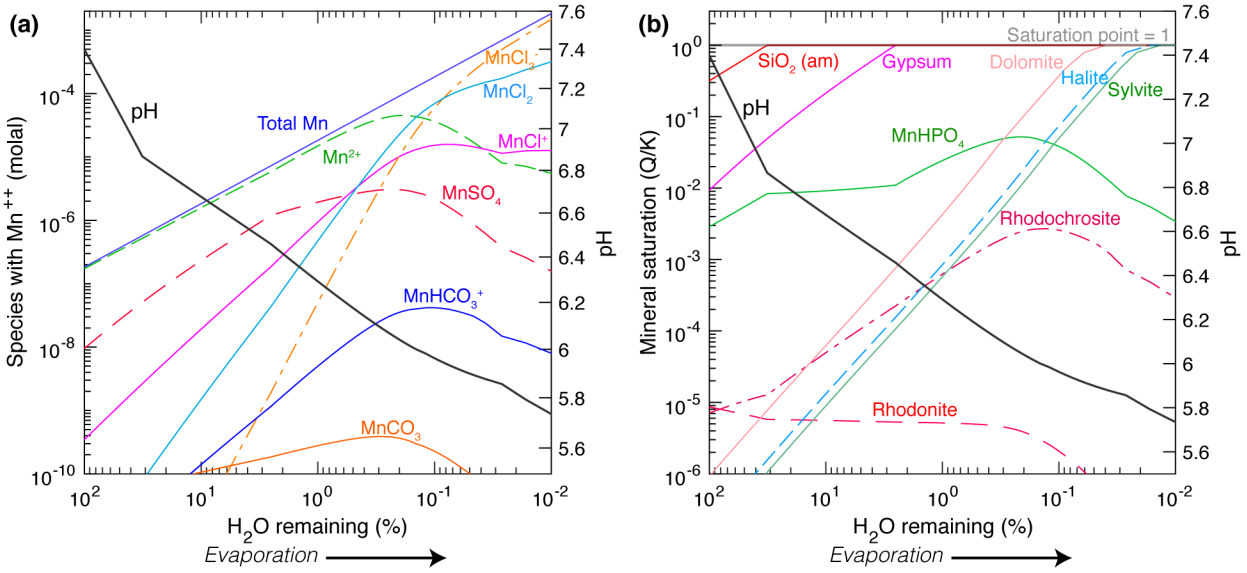

727

728 **Figure 10:** (a) Manganese-bearing species concentrations and (b) mineral saturation (Q/K) versus
729 the percent of water remaining during modeled evaporation. The reaction $H_2O(l) \Rightarrow H_2O(g)$ run
730 iteratively simulates evaporation of 99.99% of the liquid water, which proceeds from left to right
731 on the x-axis. The initial solution is adapted from analyses of aquifers in the Snake River Plains
732 Basalt in Idaho, USA (details given in Tables S4 and S5). Concentrations of aqueous Mn species
733 above 10^{-10} molal and total dissolved Mn are shown in (a). The saturation curves of Mn-bearing
734 phases and phases that reach saturation during brine evolution (amorphous silica, gypsum,
735 dolomite, halite, and sylvite) are shown in (b), where Q/K = 1 indicates saturation and Q/K < 1
736 indicates undersaturation. The model indicates that no Mn-bearing phases are saturated after
737 99.99% evaporation; all of the Mn remains in solution after 99.99% evaporation. Goethite is
738 saturated under all modeled conditions. The solution pH is shown (solid black line; right axis).
739 Secondary minerals are allowed to back-react with the solution.
740

References

Achilles, C. N., Rampe, E. B., Downs, R. T., Bristow, T. F., Ming, D. W., Morris, R. V., et al. (2020). Evidence for Multiple Diagenetic Episodes in Ancient Fluvial-Lacustrine Sedimentary Rocks in Gale Crater, Mars. *Journal of Geophysical Research: Planets*, *125*(8), e2019JE006295. https://doi.org/10.1029/2019JE006295

Agee, C. B., Wilson, N. V., McCubbin, F. M., Ziegler, K., Polyak, V. J., Sharp, Z. D., et al. (2013). Unique Meteorite from Early Amazonian Mars: Water-Rich Basaltic Breccia Northwest Africa 7034. *Science*. https://doi.org/10.1126/science.1228858

Anderson, D. E., Ehlmann, B. L., Forni, O., Clegg, S. M., Cousin, A., Thomas, N. H., et al. (2017). Characterization of LIBS emission lines for the identification of chlorides, carbonates, and sulfates in salt/basalt mixtures for the application to MSL ChemCam data. *Journal of Geophysical Research: Planets*, *122*(4), 744–770. https://doi.org/10.1002/2016JE005164

Arvidson, R. E., Squyres, S. W., Morris, R. V., Knoll, A. H., Gellert, R., Clark, B. C., et al. (2016). High concentrations of manganese and sulfur in deposits on Murray Ridge, Endeavour Crater, Mars. *American Mineralogist*, *101*(6), 1389–1405. https://doi.org/10.2138/am-2016-5599

Banham, S. G., Gupta, S., Rubin, D. M., Watkins, J. A., Sumner, D. Y., Edgett, K. S., et al. (2018). Ancient Martian aeolian processes and palaeomorphology reconstructed from the Stimson formation on the lower slope of Aeolis Mons, Gale crater, Mars. *Sedimentology*, *65*(4), 993–1042. https://doi.org/10.1111/sed.12469

Banham, S. G., Gupta, S., Rubin, D. M., Edgett, K. S., Barnes, R., Van Beek, J., et al. (2021). A Rock Record of Complex Aeolian Bedforms in a Hesperian Desert Landscape: The Stimson Formation as Exposed in the Murray Buttes, Gale Crater, Mars. *Journal of Geophysical Research: Planets*, *126*(4), e2020JE006554. https://doi.org/10.1029/2020JE006554

Berger, J. A., Schmidt, M. E., Gellert, R., Boyd, N. I., Desouza, E. D., Flemming, R. L., et al. (2017). Zinc and germanium in the sedimentary rocks of Gale Crater on Mars indicate hydrothermal enrichment followed by diagenetic fractionation. *Journal of Geophysical Research: Planets*, *122*(8), 1747–1772. https://doi.org/10.1002/2017JE005290

Berger, J. A., Gellert, R., Boyd, N. I., King, P. L., McCraig, M. A., O'Connell-Cooper, C. D., et al. (2020). Elemental Composition and Chemical Evolution of Geologic Materials in Gale Crater, Mars: APXS Results from Bradbury Landing to the Vera Rubin Ridge. *Journal of Geophysical Research: Planets*, *125*(12), e2020JE006536. https://doi.org/10.1029/2020JE006536

Berger, J. A., VanBommel, S. J. V., Clark, B. C., Gellert, R., House, C. H., King, P. L., et al. (2021). Manganese- and Phosphorus-Rich Nodules in Gale Crater, Mars: APXS Results from the Groken Drill Site. In *52nd Lunar and Planetary Science Conference* (Vol. 52, p. 2194). Retrieved from https://ui.adsabs.harvard.edu/abs/2021LPI....52.2194B/abstract

Bethke, C. M., Farrell, B., & Sharifi, M. (2020). *The Geochemist's Workbench Release 14: GWB Essentials Guide*. Champaign, Illinois: Aqueous Solutions, LLC.

Bish, D. L., Blake, D. F., Vaniman, D. T., Chipera, S. J., Morris, R. V., Ming, D. W., et al. (2013). X-ray Diffraction Results from Mars Science Laboratory: Mineralogy of Rocknest at Gale Crater. *Science*, *341*(6153), 1238932. https://doi.org/10.1126/science.1238932

Blake, D. F., Morris, R. V., Kocurek, G., Morrison, S. M., Downs, R. T., Bish, D., et al. (2013). Curiosity at Gale Crater, Mars: Characterization and Analysis of the Rocknest Sand Shadow. *Science*, *341*(6153), 1239505. https://doi.org/10.1126/science.1239505

Cabrol, N. A., Grin, E. A., Newsom, H. E., Landheim, R., & McKay, C. P. (1999). Hydrogeologic Evolution of Gale Crater and Its Relevance to the Exobiological Exploration of Mars. *Icarus*, *139*(2), 235–245. https://doi.org/10.1006/icar.1999.6099

Campbell, J. L., Perrett, G. M., Gellert, R., Andrushenko, S. M., Boyd, N. I., Maxwell, J. A., et al. (2012). Calibration of the Mars Science Laboratory Alpha Particle X-ray Spectrometer. *Space Science Reviews*, *170*(1–4), 319–340. https://doi.org/10.1007/s11214-012-9873-5

Clark, B. C., Baird, A. K., Weldon, R. J., Tsusaki, D. M., Schnabel, L., & Candelaria, M. P. (1982). Chemical composition of Martian fines. *Journal of Geophysical Research: Solid Earth*, *87*(B12), 10059–10067. https://doi.org/10.1029/JB087iB12p10059

Clark, J., Sutter, B., Archer, P. D., Ming, D., Rampe, E., McAdam, A., et al. (2021). A Review of Sample Analysis at Mars-Evolved Gas Analysis Laboratory Analog Work Supporting the Presence of Perchlorates and Chlorates in Gale Crater, Mars. *Minerals*, *11*(5), 475. https://doi.org/10.3390/min11050475

Clark, J. V., Lanza, N., Rampe, E. B., Archer, P. D., Morris, R. V., Tu, V., et al. (2021). Evolved Gas Analysis of Manganese-Bearing Phases and Implications for the Sample Analysis at Mars (SAM) Instrument on Board the Curiosity Rover in Gale Crater, Mars. In *52nd Lunar and Planetary Science Conference* (p. 1206). Retrieved from https://ui.adsabs.harvard.edu/abs/2021LPI....52.1206C

Edgar, L. A., Fedo, C. M., Gupta, S., Banham, S. G., Fraeman, A. A., Grotzinger, J. P., et al. (2020). A Lacustrine Paleoenvironment Recorded at Vera RubinRidge, Gale Crater: Overview of the Sedimentology and Stratigraphy Observed by the Mars ScienceLaboratory Curiosity Rover. *Journal of Geophysical Research: Planets*, *125*(3), e2019JE006307. https://doi.org/10.1029/2019JE006307

Fedo, C. M., Grotzinger, J. P., Gupta, S., Fraeman, A., Edgar, L. A., Edgett, K., et al. (2018). Sedimentology and stratigraphy of the Murray formation, Gale crater, Mars. In *49 th Lunar and Planetary Science Conference, Abstract* (Vol. 2078).

Foley, C. N., Economou, T., & Clayton, R. N. (2003). Final chemical results from the Mars Pathfinder alpha proton X-ray spectrometer. *Journal of Geophysical Research: Planets*, *108*(E12), 8096. https://doi.org/10.1029/2002JE002019

Forni, O., Gaft, M., Toplis, M. J., Clegg, S. M., Maurice, S., Wiens, R. C., et al. (2015). First detection of fluorine on Mars: Implications for Gale Crater's geochemistry. *Geophysical Research Letters*, *42*(4), 2014GL062742. https://doi.org/10.1002/2014GL062742

Gabriel, T. S. J., Hardgrove, C., Achilles, C., Rampe, E. B., Czarnecki, S., Rapin, W., et al. (2019). Pervasive water-rich, fracture-associated alteration halos in Gale crater, Mars. In

AGU Fall Meeting Abstracts (Vol. 43). Retrieved from http://adsabs.harvard.edu/abs/2019AGUFM.P43B..08G

Gasda, P. J., Lanza, N. L., Lamm, S. N., L'Haridon, J., Meslin, P.-Y., Forni, O., et al. (2018). Evidence of Redox Sensitive Elements Associated with Possible Shoreline Deposits in Gale Crater. *Lunar and Planetary Science Conference*, (2083), 2483.

Gellert, R., & Clark, B. C. (2015). In situ compositional measurements of rocks and soils on NASA's Mars rovers with the alpha-particle X-ray spectrometer (APXS). *Elements*, *11*, 39–44.

Gellert, R., Rieder, R., Brückner, J., Clark, B. C., Dreibus, G., Klingelhöfer, G., et al. (2006). Alpha Particle X-Ray Spectrometer (APXS): Results from Gusev crater and calibration report. *Journal of Geophysical Research*, *111*(E02S05). https://doi.org/200610.1029/2005JE002555

Gellert, R., Campbell, J. L., King, P. L., Leshin, L. A., Lugmair, G. W., Spray, J. G., et al. (2009). The Alpha-Particle-X-Ray-Spectrometer (APXS) for the Mars Science Laboratory (MSL) Rover Mission. In *Lunar Planet. Sci., XL* (p. Abstract 2364).

Groeningen, N. V., Glück, B., Christl, I., & Kretzschmar, R. (2020). Surface precipitation of Mn 2+ on clay minerals enhances Cd 2+ sorption under anoxic conditions. *Environmental Science: Processes & Impacts*, *22*(8), 1654–1665. https://doi.org/10.1039/D0EM00155D

Grotzinger, J. P., Sumner, D. Y., Kah, L. C., Stack, K., Gupta, S., Edgar, L., et al. (2014). A Habitable Fluvio-Lacustrine Environment at Yellowknife Bay, Gale Crater, Mars. *Science*, *343*(6169), 1242777. https://doi.org/10.1126/science.1242777

Grotzinger, J. P., Gupta, S., Malin, M. C., Rubin, D. M., Schieber, J., Siebach, K., et al. (2015). Deposition, exhumation, and paleoclimate of an ancient lake deposit, Gale crater, Mars. *Science*, *350*(6257), aac7575. https://doi.org/10.1126/science.aac7575

Harvie, C. E., Møller, N., & Weare, J. H. (1984). The prediction of mineral solubilities in natural waters: The Na-K-Mg-Ca-H-Cl-SO4-OH-HCO3-CO3-CO2-H2O system to high ionic strengths at 25°C. *Geochimica et Cosmochimica Acta*, *48*(4), 723–751. https://doi.org/10.1016/0016-7037(84)90098-X

Hurowitz, J. A., Grotzinger, J. P., Fischer, W. W., McLennan, S. M., Milliken, R. E., Stein, N., et al. (2017). Redox stratification of an ancient lake in Gale crater, Mars. *Science*, *356*(6341), eaah6849. https://doi.org/10.1126/science.aah6849

Kebabi, B., Terchi, S., Bougherara, H., Reinert, L., & Duclaux, L. (2017). Removal of manganese (II) by edge site adsorption on raw and milled vermiculites. *Applied Clay Science*, *139*, 92–98. https://doi.org/10.1016/j.clay.2016.12.041

King, Penelope L., & McLennan, S. M. (2010). Sulfur on Mars. *ELEMENTS*, *6*(2), 107–112. https://doi.org/10.2113/gselements.6.2.107

King, P.L., Lescinsky, D. T., & Nesbitt, H. W. (2004). The composition and evolution of primordial solutions on Mars, with application to other planetary bodies. *Geochimica et Cosmochimica Acta*, *68*, 4993–5008. https://doi.org/doi: DOI: 10.1016/j.gca.2004.05.036

Kounaves, S. P., Hecht, M. H., Kapit, J., Gospodinova, K., DeFlores, L., Quinn, R. C., et al. (2010). Wet Chemistry experiments on the 2007 Phoenix Mars Scout Lander mission:

Data analysis and results. *Journal of Geophysical Research*, *115*, 16 PP. https://doi.org/201010.1029/2009JE003424

Kounaves, S. P., Chaniotakis, N. A., Chevrier, V. F., Carrier, B. L., Folds, K. E., Hansen, V. M., et al. (2014). Identification of the perchlorate parent salts at the Phoenix Mars landing site and possible implications. *Icarus*, *232*, 226–231. https://doi.org/10.1016/j.icarus.2014.01.016

Langmuir, D. (1997). *Aqueous Environmental Geochemistry*. Prentice Hall.

Lanza, N. L., Fischer, W. W., Wiens, R. C., Grotzinger, J., Ollila, A. M., Cousin, A., et al. (2014). High manganese concentrations in rocks at Gale crater, Mars. *Geophysical Research Letters*, *41*(16), 5755–5763. https://doi.org/10.1002/2014GL060329

Lanza, N. L., Wiens, R. C., Arvidson, R. E., Clark, B. C., Fischer, W. W., Gellert, R., et al. (2016). Oxidation of manganese in an ancient aquifer, Kimberley formation, Gale crater, Mars. *Geophysical Research Letters*, *43*(14), 7398–7407. https://doi.org/10.1002/2016GL069109

Lanza, N. L., Gasda, P., Ari, E., Comellas, J., Caravaca, G., Rampe, E. B., et al. (2021). CHEMISTRY OF MANGANESE-BEARING MATERIALS AT THE GROKEN DRILL SITE, GALE CRATER, MARS. In *52nd Lunar and Planetary Science Conference*. The Woodlands, United States: Lunar and Planetary Institute. Retrieved from https://hal.archives-ouvertes.fr/hal-03143136

Lasue, J., Clegg, S. M., Forni, O., Cousin, A., Wiens, R. C., Lanza, N., et al. (2016). Observation of > 5 wt % zinc at the Kimberley outcrop, Gale crater, Mars. *Journal of Geophysical Research: Planets*, *121*(3), 338–352. https://doi.org/10.1002/2015JE004946

L'Haridon, J., Mangold, N., Fraeman, A. A., Johnson, J. R., Cousin, A., Rapin, W., et al. (2020). Iron Mobility during Diagenesis at Vera Rubin ridge, Gale Crater, Mars. *Journal of Geophysical Research: Planets*, *n/a*(n/a), e2019JE006299. https://doi.org/10.1029/2019JE006299

Martin, P. E., Farley, K. A., Baker, M. B., Malespin, C. A., Schwenzer, S. P., Cohen, B. A., et al. (2017). A Two-Step K-Ar Experiment on Mars: Dating the Diagenetic Formation of Jarosite from Amazonian Groundwaters. *Journal of Geophysical Research: Planets*, *122*(12), 2803–2818. https://doi.org/10.1002/2017JE005445

McLennan, S. M., Anderson, R. B., Bell, J. F., Bridges, J. C., Calef, F., Campbell, J. L., et al. (2013). Elemental Geochemistry of Sedimentary Rocks at Yellowknife Bay, Gale Crater, Mars. *Science*, 1244734. https://doi.org/10.1126/science.1244734

Milliken, R. E., Grotzinger, J. P., & Thomson, B. J. (2010). Paleoclimate of Mars as captured by the stratigraphic record in Gale Crater. *Geophysical Research Letters*, *37*, 6 PP. https://doi.org/201010.1029/2009GL041870

Ming, D. W., Gellert, R., Morris, R. V., Arvidson, R. E., Brückner, J., Clark, B. C., et al. (2008). Geochemical properties of rocks and soils in Gusev Crater, Mars: Results of the Alpha Particle X-Ray Spectrometer from Cumberland Ridge to Home Plate. *Journal of Geophysical Research*, *113*(E12S39), 28 PP. https://doi.org/200810.1029/2008JE003195

905 Ming, D. W., Archer, P. D., Glavin, D. P., Eigenbrode, J. L., Franz, H. B., Sutter, B., et al.
906 (2014). Volatile and Organic Compositions of Sedimentary Rocks in Yellowknife Bay,
907 Gale Crater, Mars. *Science*, *343*(6169), 1245267.
908 https://doi.org/10.1126/science.1245267

909 Mitra, K., & Catalano, J. G. (2019). Chlorate as a Potential Oxidant on Mars: Rates and Products
910 of Dissolved Fe(II) Oxidation. *Journal of Geophysical Research: Planets*, *124*(11),
911 2893–2916. https://doi.org/10.1029/2019JE006133

912 Morris, R. V., Vaniman, D. T., Blake, D. F., Gellert, R., Chipera, S. J., Rampe, E. B., et al.
913 (2016). Silicic volcanism on Mars evidenced by tridymite in high-SiO2 sedimentary rock
914 at Gale crater. *Proceedings of the National Academy of Sciences*, *113*(26), 7071–7076.
915 https://doi.org/10.1073/pnas.1607098113

916 Morrison, S. M., Downs, R. T., Blake, D. F., Vaniman, D. T., Ming, D. W., Hazen, R. M., et al.
917 (2018). Crystal chemistry of martian minerals from Bradbury Landing through Naukluft
918 Plateau, Gale crater, Mars. *American Mineralogist*, *103*(6), 857–871.
919 https://doi.org/10.2138/am-2018-6124

920 Nachon, M., Clegg, S. M., Mangold, N., Schröder, S., Kah, L. C., Dromart, G., et al. (2014).
921 Calcium sulfate veins characterized by ChemCam/Curiosity at Gale crater, Mars. *Journal*
922 *of Geophysical Research: Planets*, *119*(9), 1991–2016.
923 https://doi.org/10.1002/2013JE004588

924 Nachon, M., Mangold, N., Forni, O., Kah, L. C., Cousin, A., Wiens, R. C., et al. (2017).
925 Chemistry of diagenetic features analyzed by ChemCam at Pahrump Hills, Gale crater,
926 Mars. *Icarus*, *281*, 121–136. https://doi.org/10.1016/j.icarus.2016.08.026

927 O'Connell-Cooper, C. D., Spray, J. G., Thompson, L. M., Gellert, R., Berger, J. A., Boyd, N. I.,
928 et al. (2017). APXS-derived chemistry of the Bagnold dune sands: Comparisons with
929 Gale Crater soils and the global Martian average. *Journal of Geophysical Research:*
930 *Planets*, *122*(12), 2623–2643. https://doi.org/10.1002/2017JE005268

931 O'Connell-Cooper, C. D., Thompson, L. M., Gellert, R., Spray, J. G., Boyd, N. I., Berger, J., et
932 al. (2021). APXS Geochemistry of the Fractured Intermediate Unit (fIU) — Its
933 Relationship to Underlying Glen Torridon Units and Overlying Pediment Rocks at the
934 Greenheugh Unconformity. In *52nd Lunar and Planetary Science Conference* (p. 2405).
935 Retrieved from https://ui.adsabs.harvard.edu/abs/2021LPI....52.2405O

936 Papike, J. J., Karner, J. M., Shearer, C. K., & Burger, P. V. (2009). Silicate mineralogy of
937 martian meteorites. *Geochimica et Cosmochimica Acta*, *73*(24), 7443–7485.
938 https://doi.org/10.1016/j.gca.2009.09.008

939 Quinn, R. C., Chittenden, J. D., Kounaves, S. P., & Hecht, M. H. (2011). The oxidation-
940 reduction potential of aqueous soil solutions at the Mars Phoenix landing site.
941 *Geophysical Research Letters*, *38*(14). https://doi.org/10.1029/2011GL047671

942 Rampe, E. B., Ming, D. W., Blake, D. F., Bristow, T. F., Chipera, S. J., Grotzinger, J. P., et al.
943 (2017). Mineralogy of an ancient lacustrine mudstone succession from the Murray
944 formation, Gale crater, Mars. *Earth and Planetary Science Letters*, *471*, 172–185.
945 https://doi.org/10.1016/j.epsl.2017.04.021

946 Rampe, E. B., Blake, D. F., Bristow, T. F., Ming, D. W., Vaniman, D. T., Morris, R. V., et al.
947 (2020). Mineralogy and geochemistry of sedimentary rocks and eolian sediments in Gale
948 crater, Mars: A review after six Earth years of exploration with Curiosity. *Geochemistry*,
949 125605. https://doi.org/10.1016/j.chemer.2020.125605

950 Rice, M. S., Gupta, S., Treiman, A. H., Stack, K. M., Calef, F., Edgar, L. A., et al. (2017).
951 Geologic overview of the Mars Science Laboratory rover mission at the Kimberley, Gale
952 crater, Mars. *Journal of Geophysical Research: Planets*, *122*(1), 2016JE005200.
953 https://doi.org/10.1002/2016JE005200

954 Schmidt, M. E., Campbell, J. L., Gellert, R., Perrett, G. M., Treiman, A. H., Blaney, D. L., et al.
955 (2014). Geochemical diversity in first rocks examined by the Curiosity Rover in Gale
956 Crater: Evidence for and significance of an alkali and volatile-rich igneous source.
957 *Journal of Geophysical Research: Planets*, *119*(1), 64–81.
958 https://doi.org/10.1002/2013JE004481

959 Schmidt, M. E., Perrett, G. M., Bray, S. L., Bradley, N. J., Lee, R. E., Berger, J. A., et al. (2018).
960 Dusty Rocks in Gale Crater: Assessing Areal Coverage and Separating Dust and Rock
961 Contributions in APXS Analyses. *Journal of Geophysical Research: Planets*, *123*(7),
962 1649–1673. https://doi.org/10.1029/2018JE005553

963 Stack, K. M., Grotzinger, J. P., Lamb, M. P., Gupta, S., Rubin, D. M., Kah, L. C., et al. (2019).
964 Evidence for plunging river plume deposits in the Pahrump Hills member of the Murray
965 formation, Gale crater, Mars. *Sedimentology*, *66*(5), 1768–1802.
966 https://doi.org/10.1111/sed.12558

967 Stanley, C. R., & Madeisky, H. E. (1996). Lithogeochemical exploration for metasomatic zones
968 associated with hydrothermal mineral deposits using Pearce element ratio analysis:
969 Mineral Deposit Research Unit. *University of British Columbia, Short Course Notes*.

970 Stein, N. T., Quinn, D. P., Grotzinger, J. P., Fedo, C., Ehlmann, B. L., Stack, K. M., et al. (2020).
971 Regional Structural Orientation of the Mount Sharp Group Revealed by In Situ Dip
972 Measurements and Stratigraphic Correlations on the Vera Rubin Ridge. *Journal of*
973 *Geophysical Research: Planets*, *125*(5), e2019JE006298.
974 https://doi.org/10.1029/2019JE006298

975 Sutter, B., McAdam, A. C., Mahaffy, P. R., Ming, D. W., Edgett, K. S., Rampe, E. B., et al.
976 (2018). Evolved gas analyses of sedimentary rocks and eolian sediment in Gale Crater,
977 Mars: Results of the Curiosity rover's sample analysis at Mars instrument from
978 Yellowknife Bay to the Namib Dune. *Journal of Geophysical Research: Planets*,
979 *122*(12), 2574–2609. https://doi.org/10.1002/2016JE005225

980 Taylor, S. R., & McLennan, S. (2010). *Planetary Crusts: Their Composition, Origin and*
981 *Evolution* (1st ed.). Cambridge University Press.

982 Thompson, L. M., Schmidt, M. E., Spray, J. G., Berger, J. A., Fairén, A. G., Campbell, J. L., et
983 al. (2016). Potassium-rich sandstones within the Gale impact crater, Mars: The APXS
984 perspective. *Journal of Geophysical Research: Planets*, *121*(10), 1981–2003.
985 https://doi.org/10.1002/2016JE005055

986 Thompson, L. M., Berger, J. A., Spray, J. G., Fraeman, A. A., McCraig, M. A., O'Connell-
987 Cooper, C. D., et al. (2020). APXS-Derived Compositional Characteristics of Vera Rubin

Ridge and Murray Formation, Gale Crater, Mars: Geochemical Implications for the Origin of the Ridge. *Journal of Geophysical Research: Planets*, *125*(10), e2019JE006319. https://doi.org/10.1029/2019JE006319

Thorpe, M. T., Hurowitz, J. A., & Dehouck, E. (2019). Sediment geochemistry and mineralogy from a glacial terrain river system in southwest Iceland. *Geochimica et Cosmochimica Acta*, *263*, 140–166. https://doi.org/10.1016/j.gca.2019.08.003

Thorpe, M. T., Bristow, T. F., Rampe, E. B., Grotzinger, J. P., Fox, V. K., Bennett, K. A., et al. (2021). The Mineralogy and Sedimentary History of the Glen Torridon Region, Gale Crater, Mars. In *52nd Lunar and Planetary Science Conference* (p. 1519). Retrieved from https://ui.adsabs.harvard.edu/abs/2021LPI....52.1519T

Tosca, N. J., McLennan, S. M., Clark, B. C., Grotzinger, J. P., Hurowitz, J. A., Knoll, A. H., et al. (2005). Geochemical modeling of evaporation processes on Mars: Insight from the sedimentary record at Meridiani Planum. *Earth and Planetary Science Letters*, *240*, 122–148. https://doi.org/10.1016/j.epsl.2005.09.042

Treiman, A. H., Bish, D. L., Vaniman, D. T., Chipera, S. J., Blake, D. F., Ming, D. W., et al. (2016). Mineralogy, provenance, and diagenesis of a potassic basaltic sandstone on Mars: CheMin X-ray diffraction of the Windjana sample (Kimberley area, Gale Crater). *Journal of Geophysical Research: Planets*, *121*(1), 2015JE004932. https://doi.org/10.1002/2015JE004932

Treiman, A. H., Downs, R. T., Ming, D. W., Morris, R. V., Thorpe, M. T., Hazen, R. M., et al. (2021). Possible Detection of a Jahnsite-Whiteite Group Phosphate Mineral by MSL CheMin in Glen Torridon, Gale Crater, Mars. In *52nd Lunar and Planetary Science Conference* (p. 1200). Retrieved from https://ui.adsabs.harvard.edu/abs/2021LPI....52.1200T

VanBommel, S. J., Gellert, R., Berger, J. A., Campbell, J. L., Thompson, L. M., Edgett, K. S., et al. (2016). Deconvolution of distinct lithology chemistry through oversampling with the Mars Science Laboratory Alpha Particle X-Ray Spectrometer. *X-Ray Spectrometry*, *45*(3), 155–161. https://doi.org/10.1002/xrs.2681

VanBommel, S. J., Gellert, R., Berger, J. A., Thompson, L. M., Edgett, K. S., McBride, M. J., et al. (2017). Modeling and mitigation of sample relief effects applied to chemistry measurements by the Mars Science Laboratory Alpha Particle X-ray Spectrometer. *X-Ray Spectrometry*, *46*(4), 229–236. https://doi.org/10.1002/xrs.2755

VanBommel, S. J., Gellert, R., Boyd, N. I., & Hanania, J. U. (2019). Empirical simulations for further characterization of the Mars Science Laboratory Alpha Particle X-ray Spectrometer: An introduction to the ACES program. *Nuclear Instruments and Methods in Physics Research Section B: Beam Interactions with Materials and Atoms*, *441*, 79–87. https://doi.org/10.1016/j.nimb.2018.12.040

Vaniman, D. T., Bish, D. L., Ming, D. W., Bristow, T. F., Morris, R. V., Blake, D. F., et al. (2014). Mineralogy of a Mudstone at Yellowknife Bay, Gale Crater, Mars. *Science*, *343*(6169), 1243480. https://doi.org/10.1126/science.1243480

Wiens, R. C., Maurice, S., Lasue, J., Forni, O., Anderson, R. B., Clegg, S., et al. (2013). Pre-flight calibration and initial data processing for the ChemCam laser-induced breakdown

spectroscopy instrument on the Mars Science Laboratory rover. *Spectrochimica Acta Part B: Atomic Spectroscopy*, *82*, 1–27.

Williams, R. M. E., Grotzinger, J. P., Dietrich, W. E., Gupta, S., Sumner, D. Y., Wiens, R. C., et al. (2013). Martian Fluvial Conglomerates at Gale Crater. *Science*, *340*(6136), 1068–1072. https://doi.org/10.1126/science.1237317

Wood, W. W., & Low, W. H. (1988). *Solute geochemistry of the Snake River plain regional aquifer system, Idaho and eastern Oregon* (Report No. 1408D) (p. 91). https://doi.org/10.3133/pp1408D

Yen, A. S., Gellert, R., Schröder, C., Morris, R. V., Bell, J. F., Knudson, A. T., et al. (2005). An integrated view of the chemistry and mineralogy of martian soils. *Nature*, *436*(7047), 49–54. https://doi.org/10.1038/nature03637

Yen, A. S., Ming, D. W., Vaniman, D. T., Gellert, R., Blake, D. F., Morris, R. V., et al. (2017). Multiple stages of aqueous alteration along fractures in mudstone and sandstone strata in Gale Crater, Mars. *Earth and Planetary Science Letters*. https://doi.org/10.1016/j.epsl.2017.04.033

Yen, A. S., Morris, R. V., Ming, D. W., Schwenzer, S. P., Sutter, B., Vaniman, D. T., et al. (2021). Formation of Tridymite and Evidence for a Hydrothermal History at Gale Crater, Mars. *Journal of Geophysical Research: Planets*, *126*(3), e2020JE006569. https://doi.org/10.1029/2020JE006569